apoptosis of mesangial cells. In the glomeruli, mesangiolysis is associated with a loss of mesangial cells and capillary aneurysms. To analyze the extent of mesangiolysis, a semiquantitative mesangiolysis score was calculated in the periodic acid-Schiff stain (PAS)-stained paraffin sections. A total of 100 glomeruli were examined in each animal using the following scoring system: 0 no capillary changes; 1 capillary dilatation comprising <25% of the capillary convolute; 2 capillary dilatation comprising >25% of the capillary convolute or capillary aneurysm comprising <50% of the capillary convolute; 3 capillary aneurysm comprising 50–75% of the capillary convolute; 4 capillary aneurysm comprising >75% of the capillary convolute [9].

In *control* mice with HV GN, the mesangiolysis score was evaluated further by counting 20 glomeruli in both the medulla and cortex area. The difference between the scores was then analyzed.

Assessment of renal function

Blood urea nitrogen (BUN) and creatinine (Cr) levels were measured to assess renal function. BUN and Cr levels were analyzed by automated analysis (Hitachi 7350; Hitachi, Ibaragi, Japan) at our laboratory center. BUN and Cr levels were also measured in untreated *control* ($n = 6$) and *VHL-KO* mice ($n = 6$).

Immunohistochemical analysis

An immunohistochemical study was performed using the Ventana automated immunohistochemistry system (Discovery TM; Ventana Medical Systems, Inc., Tucson, AZ). VHL was identified by a polyclonal anti-VHL antibody, sc-5575 (1:150, BD Bioscience), VEGF by a monoclonal anti-VEGF antibody, sc-152 (1:100; Santa Cruz), CD31 by a monoclonal anti-CD31 antibody, M0823 (1:500; Dako, Hamburg, Germany) and von Willbrand Factor (vWF) by a polyclonal vWF antibody, A082 (1:500, Dako). Antigen retrieval was performed for 60 min using microwave treatment in a preheated Dako Target Retrieval Solution (pH 6.0; Dako, Glostrup, Denmark). This was followed by other steps that included inhibition of intrinsic peroxidase and blocking and reaction with a primary antibody.

In situ NO detection

Mice from each group were perfused through the left ventricle with prewarmed phosphate-buffered saline (PBS) at 37°C at a flow rate of 1 mL/min. This was followed by resection of the right atrium. After complete removal of their blood, the animals were perfused again at a flow rate of 1 mL/min for an additional 10 min with PBS that contained 0.01 mmol/L of diaminofluorescein-2 (DAF-2; Sekisui Medical, Tokyo, Japan) and 0.01 mmol/L of L-Arginine. After perfusion, the unreacted DAF-2 was removed by washing with PBS for 10 min. The NO fluorescent images of the 1-mm-thick renal tissue samples were examined using a fluorescence microscopy (Zeiss) with excitation at 490 nm and emission at 530 nm [10].

Assessment of NO involvement in protecting the kidney of VHL-KO mice from HV GN using an NOS inhibitor and an NO donor

In order to assess the involvement of NO in attenuating HV GN, we injected *VHL-KO* mice ($n = 5$) with a single bolus (12 mg/kg, i.p.) of the NOS inhibitor, N_{ω}-nitro-L-arginase (L-NNA), to 30 min prior to HV administration and then measured levels of BUN and Cr as well as mesangiolysis scores [11]. We also injected an NO donor, S-nitroso-*N*-acetyl-penicillamine (SNAP), (20 mg/kg, i.p.), 30 min before administration of HV ($n = 4$), followed by evaluation of renal function [12].

Statistical analysis

The data are expressed as the means ± SEM. The Mann–Whitney test was used to compare the two groups. In the case of multiple comparisons, differences among data were assessed by the Kruskal–Wallis test, followed by Scheffe's post hoc test. P-values <0.05 were considered statistically significant.

Results

The effects of Habu snake venom on expression of VEGF and VHL

Habu snake venom (HV) induces glomerulonephropathy (HV GN). In order to assess whether endothelial cells are targeted by HV, the expression levels of the proteins, VEGF and VHL were studied in HUVECs with and without the addition of HV (Figure 1). Initially, the VHL expression level increased >4 h period. In contrast, HV caused a gradual attenuation of VEGF expression within 8 h. However, the intact appearance of the cells suggested that HV targets endothelial cells to suppress the expression of VEGF, an endothelial cell-specific cell protective factor. Given that a comparable amount of protein was loaded in each lane, these results suggest that HV interferes specifically with endothelial VEGF expression.

Attenuation of Habu snake venom induced glomerulonephropathy in VHL-KO mice

To assess whether VHL inactivation plays a role in protecting glomerular endothelial cells in HV GN, the severity of the disease in *VHL-KO* (*VHL$^{f/f}$CreER*^{TM}) mice was compared with that in *control* (*VHL$^{f/+}$CreER*^{TM}) mice. Basal BUN levels in the HV-untreated *VHL-KO* (HV− in *VHL-KO*) (25.7 ± 1.1 mg/dL) and *control* mice (HV− in *control*) (25.2 ±1.5 mg/dL) were similar. Basal Cr levels were also not significantly different in *VHL-KO* mice (HV−) (0.25 ± 0.02 mg/dL) and *control* mice (HV−) (0.20 ± 0.03 mg/dL) (Figure 2A).

In *control* mice, HV administration (HV+ in *control*) caused a significant increase in BUN levels (60.8 ± 13.1 mg/dL) compared to nontreatment ($P < 0.05$ versus HV− in *control*) (Figure 2A). However, BUN levels in *VHL-KO* mice treated with HV (HV+ in *VHL-KO*) ($n = 11$) were significantly lower (28.4 ± 2.1 mg/dL), compared to HV-treated *control* mice ($P < 0.05$ versus HV+ in *control*)

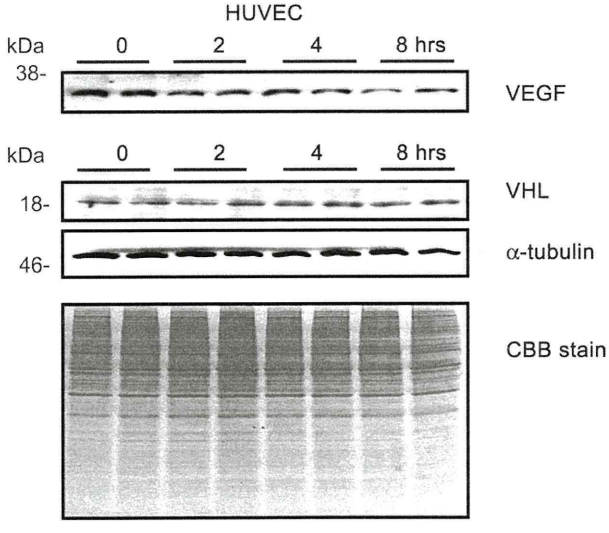

Fig. 1. Western blot analysis of VHL and VEGF expression in HUVECs with Habu snake venom. After the administration of 100 μg/mL of Habu snake venom (HV), the VHL protein expression level increases for 4 h and then stabilizes. However, HV causes a reciprocal decrease in VEGF expression level within 8 h. The application of comparable sample volumes is confirmed by Coomassie brilliant blue staining and the α-tubulin levels.

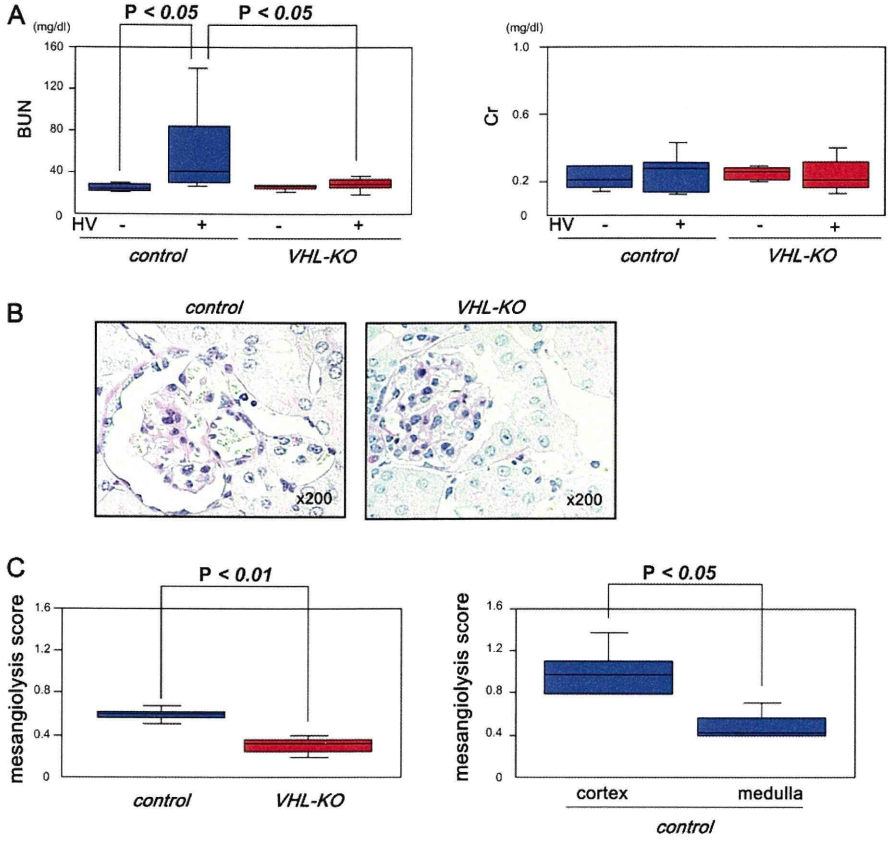

Fig. 2. Functional and pathological attenuation of Habu snake venom-induced glomerulonephropathy (HV GN) in *VHL-KO* mice. In *control* mice, HV (HV+ in *control*) causes significant increase in BUN levels compared with untreated mice ($P < 0.05$ versus HV−in *control*). In contrast, in *VHL-KO* mice with HV GN (HV+ in *VHL-KO*), BUN levels are significantly reduced, compared with *control* mice ($P < 0.05$ versus HV+ in *control*). There is no significant change in Cr levels (**A**). Glomerular damage from mesangiolysis is more evident in *control* mice (PAS stain, ×200) (**B**) with a mesangiolysis score of 0.60 ± 0.04 (**C**). In contrast, the severity of damage is significantly attenuated in *VHL-KO* mice (B), with a score of 0.31 ± 0.02 ($P < 0.001$ versus *control*) (C). In *control* mice with HV GN, the mesangiolysis score in the renal cortex (1.01 ± 0.096) is greater than that measured in the medulla (0.49 ± 0.05) ($P < 0.05$) (C).

($n = 11$) (Figure 2A). However, there was no significant difference in Cr levels between *VHL-KO* mice (HV+) (0.24 ± 0.13 mg/dL) and *control* mice (HV+) (0.25 ± 0.03 mg/dL) (Figure 2A).

The pathological features of HV GN were focal mesangiolysis (i.e. loss of mesangial cells) and capillary aneurysms in the glomeruli (Figure 2B). As a result, the glomeruli in the HV-treated *control* mice had more severe mesangiolysis with a higher mesangiolysis score of 0.60 ± 0.04. In *control* mice, further analysis of mesangiolysis in the cortex and medulla showed that injury was more evident in the cortex (mesangiolysis score of 1.01 ± 0.10) than the medulla (0.49 ± 0.05) (Figure 2C). In contrast, the severity of injury was significantly attenuated in *VHL-KO* mice, with a mesangiolysis score of 0.31 ± 0.02 ($P < 0.001$ versus *control*) (Figure 2C). Neither *VHL-KO* mice nor *control* mice had pathological lesions in the renal tubules and had negligible numbers of infiltrated inflammation cells. This suggests that VHL inactivation contributes to the protection of glomerular endothelial cells from HV-induced capillary damage.

Increased VEGF expression in glomeruli of VHL-KO mice

One week after administration of tamoxifen, VHL protein expression was reduced in the kidneys of *VHL-KO* mice compared with that in *control* mice (Figures 3A). A decrease in VHL immunoreactivity was observed, especially in the proximal tubules (Figure 3B). In contrast, VEGF expression was increased in glomeruli, especially glomerular endothelial cells, with the localization pattern of VEGF signals being comparable with that of CD31 and vWF in glomeruli from *VHL-KO* mice (Figure 3C).

In each genotype (*wild-type, hetero VHL-KO* and *control*) showing positive VEGF signals in glomeruli, with the exception of *VHL-KO*, the intensity of VEGF signals in glomeruli was remarkably reduced by HV. In contrast, VEGF signals were sustained in *VHL-KO* mice (*VHL-KO* in Figure 3D). In *VHL-KO* mice alone, VEGF immunoreactivity in glomerular capillaries was still evident with VEGF-positive signals being sustained clearly in the glomerular capillaries even following induction of HV GN. These findings were confirmed by western blot analysis (Figure 3E).

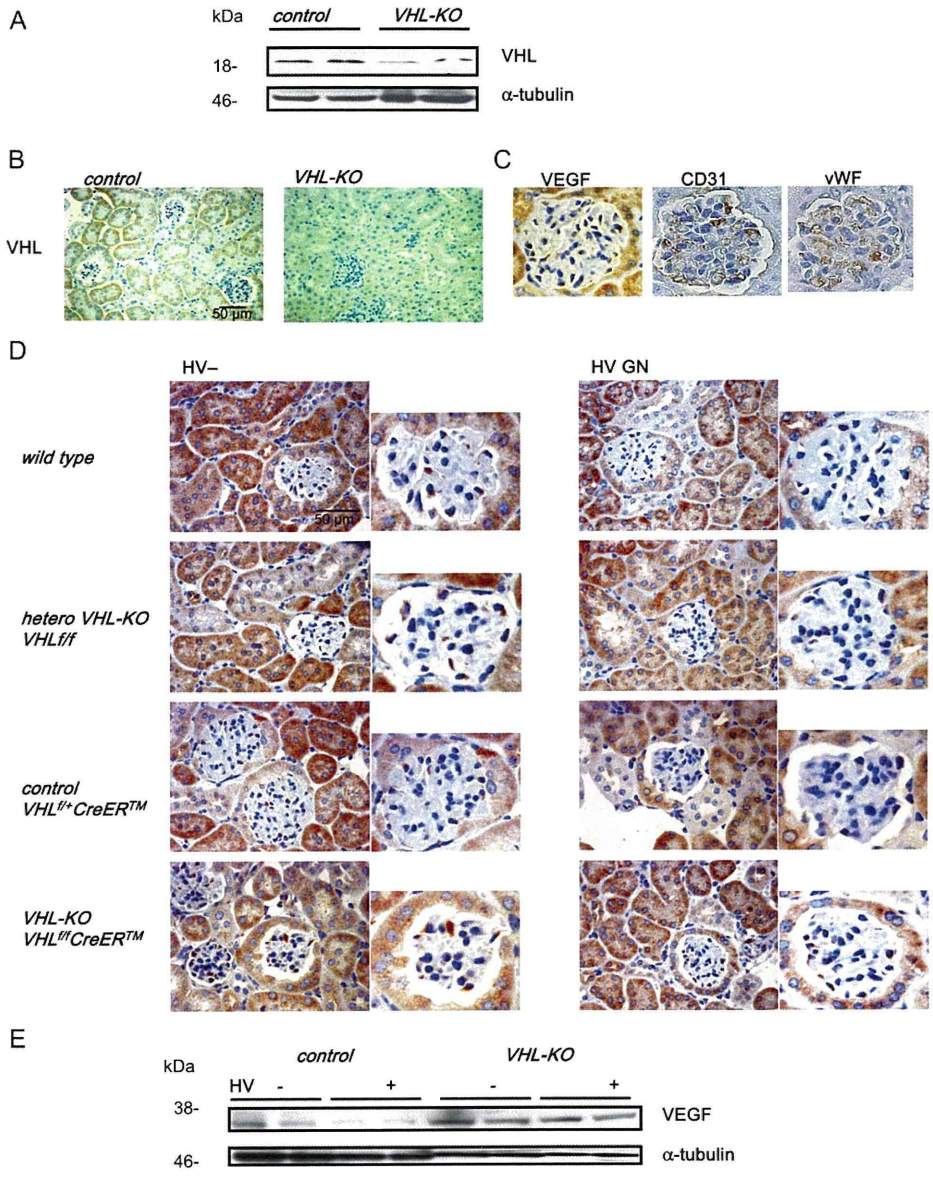

Fig. 3. VEGF is upregulated in glomerular endothelial cells in *VHL-KO* mice and VEGF signals are not attenuated in HV GN. Western blot analysis and immunohistochemical studies both demonstrate that pVHL, which is expressed predominantly in renal tubular cells, especially the proximal tubules, is decreased in *VHL-KO* mice. Two separate samples from each group are shown (**A**, **B**). The localization pattern of VEGF-positive cells is similar to that of CD31 and vWF, suggesting that VEGF is expressed in the endothelial cells (**C**). In comparison, the expression patterns of VEGF in *wild-type* mice (*wild-type*), heterogeneously VHL-deleted mice ($VHL^{del/+}$, *hetero VHL KO*) and *control* mice ($VHL^{f/+}$ *CreER*™, *control*) show that VEGF-positive signals are localized in the glomeruli. In contrast, in *VHL-KO* mice (*VHL-KO*), strong VEGF signals are detected in glomerular endothelial cells (each genotype with HV−, left panel in **D**). Glomerular VEGF is still expressed in endothelial cells of *VHL-KO* mice even following induction of HV GN. However, in *control* mice with HV GN, as well as HV-treated *wild-type* and *hetero VHL-KO*, few VEGF signals in glomeruli are detected (HV GN, right panel in D). Western blot analysis reveals that VEGF expression in the kidneys of *VHL-KO* mice with HV GN is sustained and increased compared with the HV-treated *control* mice. Two separate samples representing each group are applied for the analysis (**E**).

Upregulation of a VEGF−NO pathway in VHL-KO mice

The VEGF−NO pathway was investigated to determine the mechanisms responsible for VHL deletion-mediated glomerular protection against HV GN in *VHL-KO* mice. As VEGF reportedly triggers NO production by eNOS, the renal NO production level in *control* and *VHL-KO* mice, both not treated with HV, was initially compared using the *in situ* NO indicator DAF-2 (Figure 4A). The signal level of NO was markedly upregulated in the glomeruli and renal tubules of the *VHL-KO* mice, compared with *control* mice. This suggests that the VEGF−NO pathway is activated by VHL deletion. Western blot analysis also demonstrated enhanced expression of phosphorylated eNOS and phosphorylated Flk-1 (VEGF type 2 receptor) in *VHL-KO* mice, but showed comparable levels of total eNOS in *VHL-KO* and *control* mice (Figure 4B).

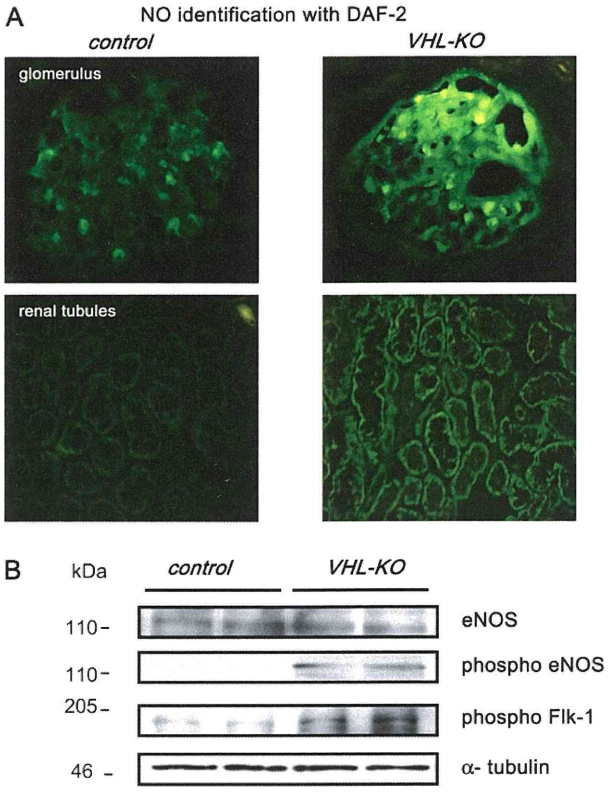

Fig 4. The increase in NO production in *VHL-KO* mice evaluated by DAF-2. In *VHL-KO* mice, the signal level of NO is upregulated markedly in the glomeruli and renal tubules compared with *control* mice. NO signals are clearly detected in endothelial cells in the glomeruli (**A**). Western blot analysis shows that phosphorylation of eNOS and Flk-1, a VEGF type 2 receptor, is upregulated in *VHL-KO* mice, with comparable levels of total eNOS being observed. Two separate samples in each group are shown (**B**).

Involvement of NO in protection of glomeruli from HV GN

HV completely eradicated NO-positive cells in the glomeruli and tubules in the *control* mice (*control*, Figure 5A). In contrast, in accordance with the effect of VHL deletion to attenuate glomerular injury, NO levels in the glomeruli of *VHL-KO* mice were also conserved in HV GN, with more NO-positive glomerular and renal tubular cells being observed (*VHL-KO* in Figure 5A). To further investigate the role of NO in protecting glomeruli from HV GN, we administered an NO donor, SNAP, to *control* mice suffering from HV GN and an NOS inhibitor, L-NNA, to *VHL-KO* mice with HV GN. The dose of each NO donor and NOS inhibitor was sufficient to modulate NO production in the kidney as assessed by DAF-2 perfusion. In *control* mice with HV GN, SNAP increased NO-positive glomeruli and renal tubules (*control* + SNAP), compared with HV GN alone (*control*). Furthermore, in *VHL-KO* mice with HV GN treated with L-NNA, the level of NO production was decreased markedly in both glomeruli and renal tubules (*VHL-KO* + L-NNA) compared with *VHL-KO* mice suffering from HV GN (*VHL-KO*).

Modulation of NO production with either an NO donor or an NOS inhibitor affected renal function in HV GN. In *control* mice with HV GN, SNAP-treated mice (SNAP+ in *control*) showed a trend toward reduced BUN and Cr levels (30.0 ± 3.2, 0.15 ± 0.01 mg/dL, respectively), although this reduction was not significantly different from that observed in non-SNAP-treated *control* mice (SNAP− in *control*) (Figure 5B). However, the mesangiolysis score of SNAP-treated *control* mice with HV GN (SNAP+ in *control*) was suppressed (0.40 ± 0.03, $P < 0.01$) compared with non-SNAP-treated mice (Figure 5C). On the other hand, L-NNA caused marked elevation in BUN and Cr levels in *VHL-KO* mice (L-NNA+ in *VHL-KO*) treated with HV compared with HV alone (L-NNA− in *VHL-KO*) (BUN 98.5 ± 16.8, Cr 0.69 ± 0.17, $P < 0.05$). As a result of the deterioration in renal function, the mesangiolysis score was markedly increased by L-NNA (1.03 ± 0.10, $P < 0.01$) (Figure 5C). These results indicate that one of the renoprotective mechanisms against HV-induced glomerular injury in *VHL-KO* mice is dependent on NO production.

Regulation of other factors enhanced in VHL-KO mice

To search for other factors that may be involved in protecting endothelial cells from glomerular injury, we investigated the protein expression levels of IL-10 and IP-10. The expression levels of IL-10 and IP-10 in *control* mice were decreased by HV, whereas the levels were sustained in *VHL-KO* mice even following HV administration (Figure 6).

Discussion

Our previous studies have revealed that coadministration of HV and angiotensin II accelerates aggravation of glomerulonephropathy in rats [1] and that upregulation of *VHL* enhances the progression of glomerulonephopathy [2]. This occurs despite *VHL* being a known substrate-docking interface that specifically recognizes prolyl-hydoroxylated HIF-1α for ubiquitin [13]. A recent study, which we carried out, also indicated that HIF-1α, HIF-2α and VEGF were upregulated in *VHL* conditional knockout (*VHL-KO*) mice, in which tamoxifen administration under normoxia initiated inactivation of pVHL, with renal tubular epithelial cells in the mice becoming resistant to ischemia–reperfusion injury [3]. This suggests that deletion of the *VHL* gene is responsible for protecting renal tubular cells. However, it remains to be established whether *VHL* gene deletion also plays a role in protecting glomerular endothelial cells from glomerulonephropathy. In this study, we induced HV GN in *VHL-KO* mice as a glomerular endothelial cell-targeted model. The mesangioproliferative nephropathy that develops in this condition represents a glomerulus-specific injury with mesangial proliferation and detachment of degenerative epithelial and endothelial cells.

Our *in vitro* studies demonstrated that expression of pVHL in endothelial cells was upregulated by HV. In contrast, VEGF expression was downregulated, indicating that the expression patterns of VHL and VEGF are reciprocally regulated and that HV targets endothelial cells and

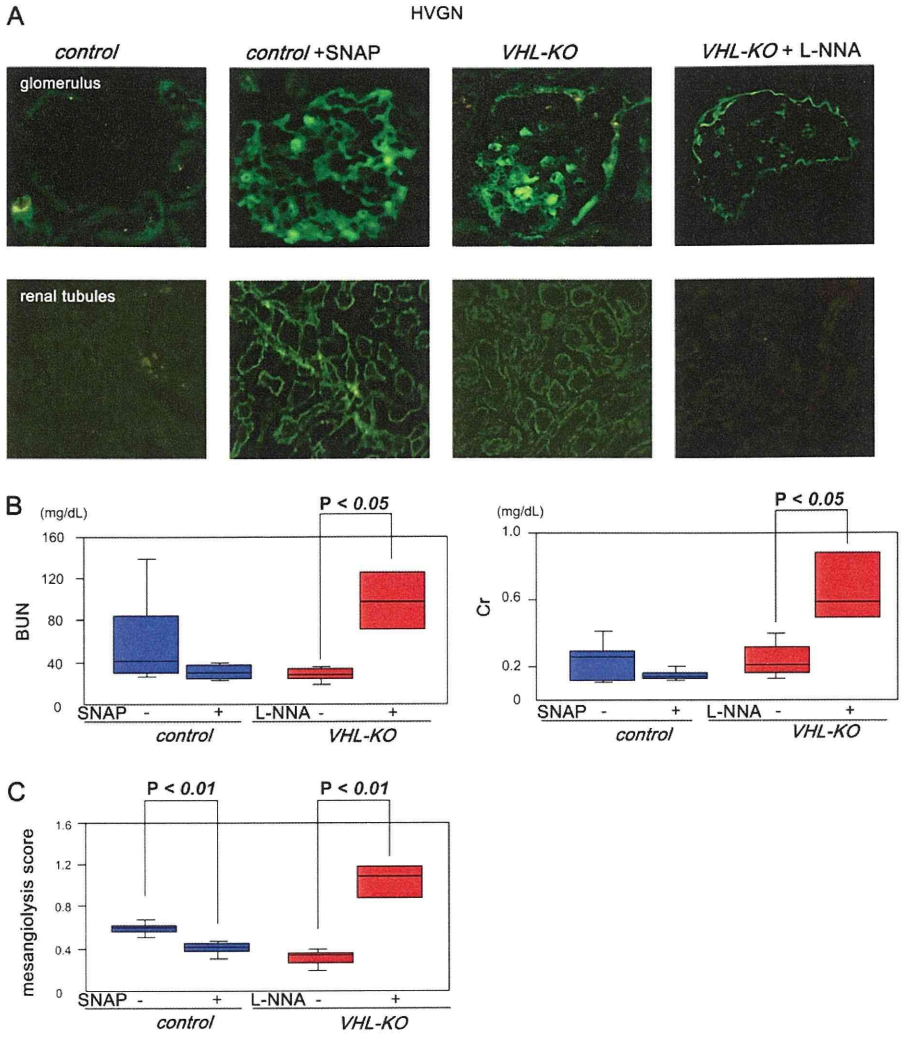

Fig. 5. The NO has a renoprotective role against HV GN in *VHL-KO* mice. In *control* mice with HV GN, NO signals are completely attenuated throughout the kidney, especially in the glomeruli (*control*). However, in *VHL-KO* mice with HV GN, NO signals are still detected in the glomeruli and renal tubules (*VHL-KO*). In *control* mice with HV GN treated with SNAP, NO signals are still detected in the glomeruli and renal tubules (+SNAP). In *VHL-KO* mice with HV GN treated with L-NNA, NO signals are completely reduced throughout the kidney, especially in the glomeruli (+L-NNA) (**A**). Comparison of *control* mice with HV GN (SNAP−) and SNAP-treated mice with HV GN (SNAP+) shows a trend of decreasing BUN and Cr levels and a significant reduction in mesangiolysis score by SNAP ($P < 0.01$) (**B**, **C**). On the other hand, the *VHL-KO* mice with HV GN treated with L-NNA (L-NNA+) shows impaired renal function with marked elevation in BUN and Cr ($P < 0.05$) and a higher mesangiolysis score ($P < 0.01$) (B, C).

modulates their gene expression. In our *in vivo* studies, *VHL-KO* mice subjected to HV showed less severe mesangiolysis than *control* mice, as demonstrated by lower mesangiolysis scores. This suggests that pVHL inactivation may ameliorate HV GN. Hass *et al.* [9] reported that HV induced a HV GN peak 1 day after injection of HV, with an average mesangiolysis score of 0.6. This score was comparable to those measured in *control* mice in our present study. Further analysis comparing the scores in the cortex and medulla revealed that the cortex was more severely injured in the control kidneys, with a greater reduction in VEGF signals in this area. As a result of HV GN, immunoreactivity for VHL was present predominantly in the renal cortex, especially in the proximal tubules. In contrast, VEGF signals, which became weaker in the cortex following induction of HV, were relatively restricted in the medulla. This finding is in agreement with our previous study that showed that pVHL is expressed exclusively in the proximal tubules. Renal function indices also confirmed the pathological differences in HV GN between *VHL-KO* and *control* mice. BUN levels were significantly decreased in *VHL-KO* mice, compared with *control* mice, while Cr levels tended to be lower, despite basal levels of BUN and Cr in two groups of mice being similar. A BUN level is rapidly affected by a kidney injury, specifically from mesangiolysis, therefore the alteration of BUN appears in the early phase of renal injury. In contrast, the level of Cr is dependent on GFR, and HV GN, unlike acute tubular necrosis, does not affect GFR in the acute phase. This might be a reason for the discrepancy.

Our *VHL-KO* mice characteristically showed enhanced VEGF expression in renal tubular cells and glomerular endothelial cells. As previously reported [14], HV causes marked suppression of VEGF expression in the glomeruli.

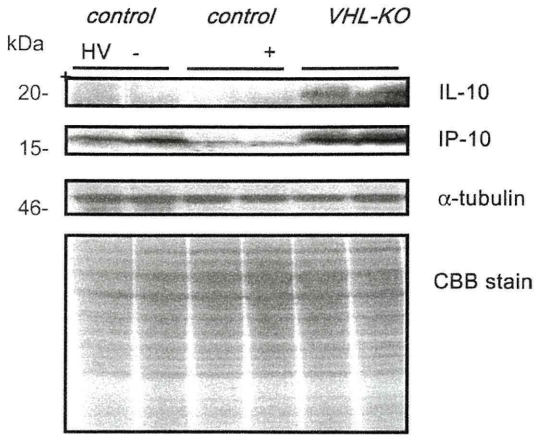

Fig. 6. Western blot analysis of IL-10 and IP-10 in the kidneys of *VHL-KO* mice. The protein expression levels of IL-10 and IP-10 are sustained in *VHL-KO* mice (HV+), compared with the *control* mice (HV+ in *control*). However, HV attenuates IL-10 and IP-10 expression in the kidney. Two separate samples in each group are shown.

Hypoxia and other stressors reportedly upregulate VEGF expression in the glomerulus [14, 15]. In several models of experimental glomerulonephropathy induced by either anti-Thy-1.1 antibody or HV, the systemic administration of VEGF also reportedly accelerates the repair of injured glomerular capillaries and prevents glomerular sclerosis [16]. Furthermore, the renoprotective effects of estrogen, which preserve the function of microvascular endothelium, are also partially mediated by VEGF [17]. It has also been reported that reduced VEGF expression is accompanied by progressive loss of glomerular and peritubular capillaries, resulting in the development of glomerulosclerosis and tubulointerstitial fibrosis, respectively [18]. Taken together, this evidence suggests that VEGF plays a major role in protecting the kidney from glomerulonephropathy.

However, upregulation of VEGF in response to renal injury does not always lead to a favorable outcome, especially in the case of VEGF treatment of the kidneys with dysfunctional endothelial cells [19]. In diabetes, VEGF is known to cause glomerular and tubular hypertrophy associated with increased urinary albumin excretion and glomerular hyperfiltration [20]. Angiotensin II also increases plasma VEGF levels and activates the local VEGF system by causing systemic hypertension and tubulointerstitial injury [21, 22]. Despite such unexpected side effects of VEGF, it has also been reported that VEGF activates NO production by increasing eNOS expression and that this balanced activation of the VEGF–NO pathway induces a survival signal in endothelial cells that sustains the function [23]. In ischemic conditions, NO contributes to protection of the kidney, whereas NO inhibitors accelerate ischemic renal injury [12, 24]. These findings indicate that as long as endothelial cell function remains intact with adequate levels of NO being produced, as demonstrated in *VHL-KO* mice, VEGF will exert balanced dual effects, including a cell-proliferative, cell-protective and NO-producing effects.

The DAF-2 perfusion and staining experiments in the present study demonstrated that NO production is increased in *VHL-KO* mice. In these mice, the intensity of NO signals was enhanced in the renal tubules and in the glomeruli, especially in endothelial cells. This suggests that NO production is increased in both types of cells. This model is therefore characterized by balanced enhancement of NO and VEGF production. As demonstrated in our study, the eNOS and VEGF type 2 receptors in *VHL-KO* mice were phosphorylated more efficiently than in *control* mice (Figure 4), a finding that supports our hypothesis.

To investigate whether NO was a crucial factor protecting glomerular cells in *VHL-KO* mice, an NO donor, SNAP, was administered to HV-treated *control* mice, and an NOS inhibitor, L-NNA, administered to HV-treated *VHL-KO* mice. Production of NO that is reduced by HV was sustained by SNAP in *control* mice even following administration with HV. On the other hand, in *VHL-KO* mice with elevated NO levels, administration of L-NNA completely blunted NO production in glomerular endothelial cells and renal tubular cells. In agreement with our findings on NO production in *control* mice, administration of SNAP was also associated with a trend of reduced BUN and Cr levels and a significant decrease in mesangiolysis score. In contrast, L-NNA suppressed NO production in *VHL-KO* mice with higher NO levels, resulting in aggravation of renal function and tissue damage.

On the basis of these findings, we consider the advantages of dual enhancement of NO production and VEGF expression in this model are as follows. As evidenced in previous reports [25–29], NO plays an anti-inflammatory role by inhibiting leukocyte migration and adhesion of platelets and monocytes to the microvascular endothelium. There is also evidence that NO protects endothelial cells from apoptosis induced by high glucose exposure and attenuates renal damage in ischemia–reperfusion injury [30]. As already mentioned, enhanced VEGF expression appears to play a pivotal role in pathological angiogenesis. However, unlike previous reports [6], our *VHL-KO* mice did not develop any capillary-rich tumors, other than hemangiomas, after *VHL* gene deletion during their lifetime.

The expression of IL-10 and IP-10, which are both known renal protective factors, was increased in the kidneys of *VHL-KO* mice. The fact that T lymphocytes produce IL-10, an immunosuppressive cytokine, led us to focus on its role as an inhibitor of tumor angiogenesis [31, 32]. IL-10 is also a potent anti-inflammatory cytokine that works partly by upregulating endothelial NO synthase [33, 34]. Although the cellular source of IL-10 was not completely investigated in the current study, our findings suggest the mechanism that attenuates HV glomerulonephropathy in *VHL-KO* mice is partly mediated by NO production via VEGF and/or IL-10. Furthermore, IP-10, which is also upregulated in *VHL-KO* mice, reportedly competes against the effects of VEGF and negatively modulates angiogenesis, resulting in the death of cells in newly formed blood vessels. This suggests that IP-10 may regulate against excessive angiogenesis [35]. The mechanism responsible for upregulating IP-10 expression may therefore be a response to the overexpression of VEGF and may counteract the actions of VEGF, which is markedly expressed in *VHL-KO* mice. IP-10 also reportedly possesses an inhibitory effect on tubular cell proliferation *in vivo* and

in vitro [36]. Consequently, upregulation of IP-10 may protect glomerular and interstitial tissue in the kidney from HV.

The side effects of chronic *VHL* knockdown were never observed pathologically or morphologically in the kidney and other organs in our *VHL-KO* mice. Further study is therefore needed to investigate the chronic phenotypes of *VHL* gene deletion.

In conclusion, this study indicates that VHL deletion activates the NO–VEGF axis properly to salvage glomerular endothelial cells from glomerulonephropathy.

Acknowledgements. This research was supported by Grants-in-Aid from the Japan Society for the Promotion of Science (19590251, 21590283).

Conflict of interest statement. None declared.

References

1. Kudo Y, Kakinuma Y, Mori Y *et al.* Hypoxia-inducible factor-1alpha is involved in the attenuation of experimentally induced rat glomerulonephritis. *Nephron Exp Nephrol* 2005; 100: e95–e103
2. Kudo Y, Kakinuma Y, Iguchi M *et al.* Modification in the von Hippel-Lindau protein is involved in the progression of experimentally induced rat glomerulonephritis. *Nephron Exp Nephrol* 2007; 106: e97–e106
3. Iguchi M, Kakinuma Y, Kurabayashi A *et al.* Acute inactivation of the VHL gene contributes to protective effects of ischemic preconditioning in the mouse kidney. *Nephron Exp Nephrol* 2008; 110: e82–e90
4. Richard D, Berra E, Pouyssegur J. Nonhypoxic pathway mediates the induction of hypoxia-inducible factor-1alpha in vascular smooth muscle cells. *J Biol Chem* 2000; 275: 26765–26771
5. Nakagawa T. Uncoupling of the VEGF-endothelial nitric oxide axis in diabetic nephropathy: an explanation for the paradoxical effects of VEGF in renal disease. *Am J Physiol Renal Physiol* 2007; 292: F1665–F1672
6. Ma W, Tessarollo L, Hong S *et al.* Hepatic vascular tumors, angiectasis in multiple organs, and impaired spermatogenesis in mice with conditional inactivation of the VHL gene. *Cancer Res* 2003; 63: 5320–5328
7. Kakinuma Y, Ando M, Kuwabara M *et al.* Acetylcholine from vagal stimulation protects cardiomyocytes against ischemia and hypoxia involving additive non-hypoxic induction of HIF-1alpha. *FEBS Lett* 2005; 579: 2111–2118
8. Cattell V, Bradfield J. Focal mesangial proliferative glomerulonephritis in the rat caused by habu snake venom. A morphologic study. *Am J Pathol* 1977; 87: 511–524
9. Haas C, Câmpean V, Kuhlmann A *et al.* Analysis of glomerular VEGF mRNA and protein expression in murine mesangioproliferative glomerulonephritis. *Virchows Arch* 2007; 450: 81–92
10. Kuwabara M, Kakinuma Y, Ando M *et al.* Nitric oxide stimulates vascular endothelial growth factor production in cardiomyocytes involved in angiogenesis. *J Physiol Sci* 2006; 56: 95–101
11. Park KM, Byun JY, Kramers C *et al.* Inducible nitric-oxide synthase is an important contributor to prolonged protective effects of ischemic preconditioning in the mouse kidney. *J Biol Chem* 2003; 278: 27256–27266
12. Shin IC, Kim HC, Swanson J *et al.* Anxiolytic effects of acute morphine can be modulated by nitric oxide systems. *Pharmacology* 2003; 68: 183–189
13. Maynard MA, Ohh M. von Hippel-Lindau tumor suppressor protein and hypoxia-inducible factor in kidney cancer. *Am J Nephrol* 2004; 24: 1–13
14. Abe-Yoshio Y, Abe K, Miyazaki M *et al.* Involvement of bone marrow-derived endothelial progenitor cells in glomerular capillary repair in habu snake venom-induced glomerulonephritis. *Virchows Arch* 2008; 453: 97–106
15. Iruela-Arispe L, Gordon K, Hugo C *et al.* Participation of glomerular endothelial cells in the capillary repair of glomerulonephritis. *Am J Pathol* 1995; 147: 1715–1727
16. Kelly D, Hepper C, Wu L *et al.* Vascular endothelial growth factor expression and glomerular endothelial cell loss in the remnant kidney model. *Nephrol Dial Transplant* 2003; 18: 1286–1292
17. Kang D, Yu E, Yoon K *et al.* The impact of gender on progression of renal disease: potential role of estrogen-mediated vascular endothelial growth factor regulation and vascular protection. *Am J Pathol* 2004; 164: 679–688
18. Kang D, Hughes J, Mazzali M *et al.* Impaired angiogenesis in the remnant kidney model: II. Vascular endothelial growth factor administration reduces renal fibrosis and stabilizes renal function. *J Am Soc Nephrol* 2001; 12: 1448–1457
19. Cooper M, Vranes D, Youssef S *et al.* Increased renal expression of vascular endothelial growth factor (VEGF) and its receptor VEGFR-2 in experimental diabetes. *Diabetes* 1999; 48: 2229–2239
20. de Vriese A, Tilton R, Elger M *et al.* Antibodies against vascular endothelial growth factor improve early renal dysfunction in experimental diabetes. *J Am Soc Nephrol* 2001; 12: 993–1000
21. Masuda Y, Shimizu A, Mori T *et al.* Vascular endothelial growth factor enhances glomerular capillary repair and accelerates resolution of experimentally induced glomerulonephritis. *Am J Pathol* 2001; 159: 599–608
22. Zhao Q, Egashira K, Inoue S *et al.* Vascular endothelial growth factor is necessary in the development of arteriosclerosis by recruiting/activating monocytes in a rat model of long-term inhibition of nitric oxide synthesis. *Circulation* 2002; 105: 1110–1115
23. Ziche M, Morbidelli L, Choudhuri R *et al.* Nitric oxide synthase lies downstream from vascular endothelial growth factor-induced but not basic fibroblast growth factor-induced angiogenesis. *J Clin Invest* 1997; 99: 2625–2634
24. Chander V, Chopra K. Protective effect of nitric oxide pathway in resveratrol renal ischemia-reperfusion injury in rats. *Arch Med Res* 2006; 36: 19–26
25. Ialenti A, Ianaro A, Maffa P *et al.* Nitric oxide inhibits leukocyte migration in carrageenin-induced rat pleurisy. *Inflamm Res* 2000; 49: 411–427
26. Cuzzocrea S, Chatterjee PK, Mazzon E *et al.* Role of induced nitric oxide in the initiation of the inflammatory response after postischemic injury. *Shock* 2002; 18: 169–176
27. Ho FM, Liu SH, Liau CS *et al.* Nitric oxide prevents apoptosis of human endothelial cells from high glucose exposure during early stage. *J Cell Biochem* 1999; 75: 258–263
28. Kim HW, Greenburg AG. Nitric oxide scavenging, alone or with nitric oxide synthesis inhibition, modulates vascular hyporeactivity in rats with intraperitoneal sepsis. *Shock* 2002; 17: 423–426
29. Radomski MW, Palmer RMJ, Moncada S. Endogenous nitric oxide inhibits human platelet adhesion to vascular endothelium. *Lancet* 1987; 2: 1057–1058
30. Milsom A, Patel N, Mazzon E *et al.* Role for endothelial nitric oxide synthase in nitrite-induced protection against renal ischemia-reperfusion injury in mice. *Nitric Oxide* 2010; 22: 141–148
31. Kohno T, Mizukami H, Suzuki M *et al.* Interleukin-10-mediated inhibition of angiogenesis and tumor growth in mice bearing VEGF-producing ovarian cancer. *Cancer Res* 2003; 63: 5091–5094
32. Elenkov I, Chrousos G. Stress hormones, proinflammatory and anti-inflammatory cytokines, and autoimmunity. *Ann N Y Acad Sci* 2002; 966: 290–303
33. Cattaruzza M, Słodowski W, Stojakovic M *et al.* Interleukin-10 induction of nitric-oxide synthase expression attenuates cd40-mediated interleukin-12 synthesis in human endothelial cells. *J Biol Chem* 2003; 278: 37874–37880
34. Silvestre J, Mallat Z, Duriez M *et al.* Antiangiogenic effect of interleukin-10 in ischemia-induced angiogenesis in mice hindlimb. *Circ Res* 2000; 87: 448–452
35. Furuichi K, Wada T, Kitajima S *et al.* IFN-inducible protein 10 (CXCL10) regulates tubular cell proliferation in renal ischemia-reperfusion injury. *Nephron Exp Nephrol* 2008; 109: c29–c38
36. Bodnar R, Yates C, Rodgers M *et al.* IP-10 induces dissociation of newly formed blood vessels. *J Cell Sci* 2009; 122: 2064–2077

Received for publication: 22.7.10; Accepted in revised form: 10.3.11

In the Spotlight: BioInstrumentation

Ken-ichi Yamakoshi, *Member, IEEE*

OVER the major part of the last century medical instruments based on a variety of principles and technologies were developed for the measurement of physiological variables to aid diagnosis and medical treatment in the hospital as well as in the out-patient clinic. More latterly, however, there has been a growing interest and effort to obtain vital signs during normal daily life to achieve healthcare management at home. In order to realize this goal, it appears necessary to develop automatic means for the acquisition of the required physiological data and to implement this in a noninvasive fashion. It might also be of value to people in their home during daily routines to assist them by monitoring the usage of the home services and facilities in a fully automated manner.

The concept of this human support system, including features aimed at achieving home healthcare, is generally referred to as a "smart home" or "smart house." This has several elements, in particular: 1) as far as possible measurements should be made automatically, with only minimal operation required by the subjects; 2) monitoring should be continuous and around the clock; 3) the intended subjects might be elderly, physically or mentally challenged, at risk of illness, but not necessarily having an existing medical condition.

The development of the smart home through modern technological advances has progressed remarkably, and the present "In the Spotlight" column focuses on the various topics within this research area and briefly introduces several trials where recent advances have been made.

I. Progress in the Emergence of the Smart Home

The "smart home" or "smart house" is an intelligent residential environment to subserve inhabitants' needs and has been considered to be one of the most desirable dwellings of the future [1]. The first clear description of the smart home concept appears to have been presented by M. Weiser in 1991 [2]. The vision was of a place where many computers and electronic devices with wire/wireless communications were installed to support living environments. This work has also been well recognized as possibly the first proposal of "ubiquitous computing" or "pervasive computing." The author's concept is neatly encapsulated in the subtitle of the report, as *"Specialized elements of hardware and software, connected by wires, radio waves and infrared, will be so ubiquitous that no one will notice their presence."* This proposal included almost all of the constituent elements of the current smart home trials (and also ubiquitous computing), with the exception of the specific provision of healthcare services. After this key published work, many proposals have been made to create smart homes with modern technologies.

Currently, an important aspect of smart homes under discussion and being developed is the inclusion of healthcare services. Of relevance here is the activity of CENELEC (European Committee for Electro-technical Standardization), which has produced a roadmap for an integrated set of standards for the "smart home [3]." This roadmap includes several applications of services such as broadband communication, multimedia and entertainment, safety and security, home automation, energy management, and, significantly, telecare and healthcare. With regard to the implementation of smart home designs the recent and on-going advances within information communication technology (ICT) and pervasive computing have yielded new devices with appropriate characteristics [1]: 1) miniature—devices can be blended with or disappear into the environment; 2) communication—devices can communicate with other equipment; 3) autonomy—devices can work autonomously. These characteristics are also ideal for use in smart home healthcare systems, and this review will therefore focus on current technologies of the smart home incorporating healthcare services.

II. Smart Home for Healthcare

The concept of healthcare within smart homes often arises from a recognition of the growing importance of the so-called aging society within the community, countries or, indeed, the

Manuscript received September 21, 2011; accepted October 11, 2011. Date of publication October 19, 2011; date of current version January 06, 2012.

K. Yamakoshi is with the College of Science & Engineering and the Graduate School of Natural Science & Technology, Kanazawa University, Kakuma, Kanazawa 920-1192, Japan (e-mail: yamakosi@t.kanazawa-u.ac.jp).

Digital Object Identifier 10.1109/RBME.2011.2172599

whole world. A smart home equipped with sensors, actuators, and biomedical instruments may provide a better and more cost-effective living environment for elderly care in a person's own home. This could be achieved in an unrestrained manner, offering better independence, helping to maintain a good health condition as well as preventing social isolation. This system would also have networking means for communication between devices in the home and with a remote center and/or a family living remotely. Chan *et al.* gave a good review of this concept, introducing 13 smart home projects in the USA, the U.K. and Japan [4]. In addition, it is pertinent that these authors discussed in detail both advantages and disadvantages of the approach. The disadvantages identified by them are as follows: The smart home 1) involves a technology-push type rather than a demand-pull approach; 2) lacks interchangeability between a healthcare professional person and the system; 3) has difficulties of acceptance due to social, ethical and legal barriers; 4) requires considerable time and cost to operate the system; 5) can have privacy problems. It is also pointed out that it is doubtful if the present smart home technologies can truly lead to reduced healthcare costs in the future [5]. Although the above issues are open to debate, further evaluation of these possible disadvantages should be carried out carefully because of the impact on what is a seminal issue with implications for the practical realization of smart homes in the near future.

III. Bioinstrumentation for the Smart Home

Biomedical instrumentation constitutes an important, indeed essential element of the smart home [1], [3], [4], as reviewed recently by Ding *et al.* [6]. These authors categorized sensor technologies for the smart home into five types: 1) simple binary sensors (SBSs), 2) video cameras (VCs), 3) radio frequency identification devices (RFID), 4) infrastructure mediated systems (IMSs), and 5) other sensors. Motion detectors, pressure sensors, and contact switches are used as SBSs, indicating the presence of a human or their movement with a single digit "1" or "0." IMSs utilize motion sensors to determine human behavior in the house, these being positioned in such infrastructures as central heating, ventilation, air conditioning and so on. Other sensors used include environmental sensors to detect humidity, temperature, light and barometric pressure, and a microphone or a pneumatic strip installed under the bed linen to detect presence, respiration, cardiac pulse and body movements in the bed.

Skubic *et al.* have reported their efforts to develop smart home-based bioinstrumentation [7]. They investigated the construction of sensor-network systems for monitoring the behavior of elderly people in their own homes situated within the TigerPlace, an aging-in-place community located in Columbia, MO, USA [8]. The authors equipped and installed their network systems in 17 apartments and reported the operational monitoring status, which lasted in some cases more than two years [7]. The sensors used in this work were quite standard motion sensors, video sensors, and a bed sensor capable of capturing restlessness in sleep, cardiac pulse and respiration rates. The bed sensor consisted of a hydraulic sensor placed beneath a standard mattress [9].

An appropriate combination of signals obtained from several SBSs is able to give quite effective information about human behavior at home [4], [10], [11]. In general, however, it is difficult to perform a detailed analysis of human behavior due to the lack of standardization or generalization of the analysis methodology, and the use of different sensor positioning in the home, as well as the performance specification of sensors to be used. Recently, Hong *et al.* tried to overcome these problems [12]. They described a general ontology network of human activity using sensors positioned appropriately, giving the ontology-based activity estimation in the kitchen as an example. They also introduced the Dempster–Shafer theory of evidence [13] for addressing uncertainty between human behavior and the sensor outputs, and demonstrated the human activity estimation from the sensor outputs. It is interesting to note that their ontology network approach with the Dempster–Shafer theory has the potential to establish the standardization/generalization of the analyses from outputs of SBSs that are properly placed in the house.

In the sensing systems mentioned above, however, physiological measurement techniques have not been employed successfully to obtain such vital signs as ECG, body temperature and blood pressure. Nevertheless, directly relevant advances in physiological measurement techniques, with apparatus installed in household equipment, have been reported [14]–[20]. The development of these systems has arisen from the need for healthcare at home and is an independent approach to the smart home-based development. The main focus has been to design systems to monitor physiological variables in a fully automated manner, without the need either to attach any biological sensors to the body or for individuals to carry out any operations, simply using home facilities such as a bed, a bathtub, and a rest room. Similar to the concept of the smart home, the techniques used in the physiological measurement approach do not disturb normal daily activities, and thus the monitoring is done in an unconstrained manner, so-called "non-conscious physiological monitoring." This means that a subject does not need to be aware of the measurement being made, and the physiological data collected and stored are truly representative of normal daily living. In fact, this concept could also be applicable and useful for patient monitoring in a hospital room [17], [20].

With the nonconscious physiological monitoring system during sleeping the array of sensors incorporated within the bed can collect useful physiological data. This includes the cardiac pulse, respiration and snoring using a flat-type under-pillow sensor with vinyl tubes filled with silicone oil [17]–[20]. Also derived are a body surface contact-pressure distribution map together with body movements using a bed sheet-type pressure sensor with 2D-distributed multi-pressure elements [20]. For the care of the elderly there is a risk of drowning in the bathtub and a reliable alarm is needed. Therefore the bathtub monitoring system allows the simultaneous detection of the ECG together with respiration signals from electrodes embedded into the wall of the bathtub.

In the toilet monitoring system a highly accurate weighing scale device is installed in the lavatory floor around the toilet bowl. This is able to measure body and excretion weight and urination rate together with the ballistocardiogram (a small body weight change produced by cardiac blood ejection; [14], [15], [21]). Also, a system built into the toilet seat allows the blood

pressure to be measured [16], [17], [20]. Just recently, these authors have developed a network system that connects with each facility monitoring system using a Local Area Network (LAN). This network system is also supervised from another site (data server center) *via* a public Wide Area Network (WAN) with appropriate security, so as to consolidate individual healthcare information [20].

IV. Summary and Future Aspects of the Smart Home

The emergence and recent developments of the smart home have been briefly introduced in this review. Initial developments of smart homes comprised of computer-based housing to support elderly and challenged persons at home during daily living through the automatic monitoring of the usage of home infrastructures. In light of the rapid growth of the aging society, which has created what might be regarded as a longevity crisis, healthcare is also one of the most serious and worldwide issues to address. From this background, the smart home with healthcare management has rapidly been pushed into the spotlight.

Utilizing ICT technologies could also dramatically facilitate this approach, with the prospects of achieving smart home healthcare in an integrated manner [22], [23]. For example, Yuce [24] showed a very promising implementation approach for healthcare monitoring systems using W-BAN (wireless body area network). In addition, the smart home with ICT technologies has strong potential to realize fully a human support system including healthcare both in- and out of the house [18]–[20], [25], that is, to achieve a ubiquitous bioinstrumentation human support system (u-BHS).

To promote such u-BHS further, the establishment of an appropriate social infrastructure that meets the needs of human life support is urgently needed. Efforts to produce much more human-friendly and universally accepted u-BHSs, where a number of practical problems still remain, are likely to be resolved through the recent dramatic advances in the integration of microelectronic, micromechanical as well as ICT technologies.

Acknowledgment

The author wishes to thank Dr. M. Ogawa, Kanazawa University, for his elaborate efforts on assisting in the survey of publications relating to current smart home issues. He is also grateful to Professor P. Rolfe, Harbin Institute of Technology, China, and OBH Ltd., UK., for his help in preparing the manuscript.

References

[1] , M. A. Al-Qutayri, Ed., *Smart Home Systems*. Vukovar, Croatia: In-Tech, 2010, pp. 1–16.

[2] M. Weiser, "The computer for the 21st century," *Scientific Amer.*, vol. 265, no. 3, pp. 66–75, 1991.

[3] Production of a Roadmap for an Integrated Set of Standards for Smarthouse and Systems Related to it and an Open Event CENELEC, 2008 [Online]. Available: ftp://ftp.cencenelec.eu/CENELEC/SmartHouse/SmartHouseRoadmap.pdf

[4] M. Chan, E. Campo, D. Estève, and J. Y. Fourniols, "Smart homes—Current features and future perspectives," *Maturitas*, vol. 64, no. 2, pp. 90–97, 2009.

[5] P. N. T. Wells, "Can technology truly reduce health care costs?," *IEEE Eng. in Med. and Biol. Mag.*, vol. 22, no. 1, pp. 20–25, 2003.

[6] D. Ding, R. A. Cooper, P. F. Pasquina, and L. Fici-Pasquina, "Sensor technology for smart homes," *Maturitas*, vol. 69, no. 2, pp. 131–136, 2011.

[7] M. Skubic, G. Alexander, M. Popescu, M. Rantz, and J. Keller, "A smart home application to eldercare: Current status and lessons learned," *Technology and Health Care*, vol. 17, no. 3, pp. 183–201, 2009.

[8] Independent living by Americare & The Sinclair School of Nursing TigerPlace, 2011 [Online]. Available: http://www.americareusa.net/independent_living/Columbia_MO/zip_65201/americare/1335

[9] D. Heise, L. Rosales, M. Skubic, and M. J. Devaney, "Refinement and evaluation of a hydraulic bed sensor," in *Proc. 33rd Annu. Int. Conf. IEEE Eng. Med. Biol.*, 2011, pp. 4356–4360.

[10] M. W. Raad and L. T. Yang, "A ubiquitous smart home for elderly," *Info. Syst. Front.*, vol. 11, no. 5, pp. 529–536, 2009.

[11] J. Neuhaeuser, J. Diehl-Schmid, and T. C. Lueth, "Evaluation of a radio based ADL interaction recognition system in a day hospital for old age psychiatry with healthy probands," in *Proc. 33rd Annu. Int. Conf. IEEE Eng. Med. Biol.*, 2011, pp. 1814–1818.

[12] X. Hong, C. Nugent, M. Mulvenna, S. McClean, B. Scotney, and S. Devlin, "Evidential fusion of sensor data for activity recognition in smart homes," *Pervasive and Mobile Computing*, vol. 5, no. 3, pp. 236–252, 2009.

[13] G. Shafer, *A Mathematical Theory of Evidence*. Princeton, NJ: Princeton Univ. Press, 1976.

[14] K. Yamakoshi, M. Kuroda, S. Tanaka, I. Yamaguchi, and A. Kawarada, "Non-conscious and automatic acquisition of body and excreta weight together with ballistocardiogram in a lavatory," in *Proc. 18th Annu. Int. Conf. IEEE Eng. Med. Biol.*, 1996, pp. 10–11.

[15] K. Yamakoshi, "Unconstrained physiological monitoring in daily living for health care," *Front. Med. & Biol. Eng.*, vol. 10, no. 3, pp. 239–259, 2000.

[16] S. Tanaka, M. Nogawa, and K. Yamakoshi, "Fully automatic system for monitoring blood pressure from a toilet-seat using the volume-oscillometric method," in *Proc. 27th Annu. Int. Conf. IEEE Eng. Med. Biol.*, 2005, pp. 3939–3941.

[17] K. Motoi, M. Ogawa, H. Ueno, Y. Kuwae, A. Ikarashi, T. Yuji, Y. Higashi, S. Tanaka, T. Fujimoto, H. Asanoi, and K. Yamakoshi, "A fully automated health-care monitoring at home without attachment of any biological sensors and its clinical evaluation," in *Proc. 31st Annu. Int. Conf. IEEE Eng. Med. Biol.*, 2009, pp. 4323–4326.

[18] K. Yamakoshi, "Current status of non-invasive bioinstrumentation for healthcare," *Sens. and Mater.*, vol. 23, no. 1, pp. 1–20, 2011.

[19] K. Motoi, A. Ikarashi, S. Tanaka, and K. Yamakoshi, "Ubiquitous healthcare monitoring for daily life," in *Distributed Diagnosis and Home Healthcare*, U. R. Acharya, Ed. *et al.* Valencia, CA: American Scientific, 2011.

[20] K. Motoi, S. Taniguchi, T. Yuji, M. Ogawa, N. Tanaka, K. Hata, M. Baek, H. Ueno, M. Wakugawa, T. Sonoda, S. Fukunaga, Y. Higashi, K. Matsumura, T. Yamakoshi, S. Tanaka, T. Fujimoto, H. Asanoi, and K. Yamakoshi, "Development of a ubiquitous healthcare monitoring system combined with non-conscious and ambulatory physiological measurements and its application to medical care," in *Proc. 33rd Annu. Int. Conf. IEEE Eng. Med. Biol.*, 2011, pp. 8211–8214.

[21] K. Yamakoshi, "In the spotlight: Bioinstrumentation," *IEEE Rev. Biomed. Eng.*, vol. 2, pp. 2–5, 2009.

[22] C. Chen and C. Pomalaza-Raez, "Implementing and evaluating a wireless body sensor system for automated physiological data acquisition at home," *Int. J. Comput. Sci. Info. Technol.*, vol. 2, no. 3, pp. 24–38, 2010.

[23] H. Huo, Y. Xu, H. Yan, S. Mubeen, and H. Zhang, "An elderly health care system using wireless sensor networks at home," in *Proc. 3rd Int. Conf. Sensor Technologies and Applicat.*, 2009, pp. 158–163.

[24] M. R. Yuce, "Implementation of wireless body area networks for healthcare systems," *Sens. Actu. A: Physical*, vol. 162, no. 1, pp. 116–129, 2010.

[25] J. Kim, S. Cho, and S. J. Kim, "Preliminary studies to develop a ubiquitous computing and health-monitoring system for wheelchair users," in *Proc. 3rd Int. ICST Conf. Body Area Netw.*, 2008, doi: 10.4108/ICST.BODYNETS2008.2974.

手　術　第65巻 第4号　平成23年4月15日発行　別刷

Operation

特集　センチネルノード―各領域の進歩―

Hyper Eye Medical System を用いた乳癌センチネルリンパ節生検手技

杉本　健樹　花﨑　和弘　佐藤　隆幸

金　原　出　版　株　式　会　社

Hyper Eye Medical System を用いた乳癌センチネルリンパ節生検手技

杉本 健樹* 花﨑 和弘*2 佐藤 隆幸*3

はじめに

乳癌のセンチネルリンパ節同定法として，もっとも標準的な色素法とラジオアイソトープ（RI）法に加え，インドシアニングリーン（ICG）の近赤外線蛍光を可視化する特殊なカメラを用いた方法はすでに実用化されている[1)2)]。既存のシステムのなかで，本邦で乳癌センチネルリンパ節生検に汎用されているのは浜松ホトニクス社製の近赤外線カメラシステム Photo-dynamic Eye（PDE）である。このシステムはICG近赤外蛍光を暗視野でモノクロの画面上に描出する。このため，蛍光を観察する際には手術室の消灯が必要であることや蛍光を発するリンパ管・リンパ節は可視化できるもののモノクロ画面では周囲組織の観察は十分に行えないことなどから，リアルタイムの手術ナビゲーターとしては不満の残る部分がある。

われわれは，近赤外線に対して超高感度のCCDセンサーと可視光を減弱させる特殊な光学フィルターを組み合わせることで，明視野のカラー画面にICG近赤外蛍光を描出できる近赤外蛍光カラーカメラシステム hyper eye medical system（HEMS）（瑞穂医科工業製）を開発した。すでに，試作機の心・血管外科領域での有用性を報告し[3)]，ICG近赤外線蛍光の医療応用の分野では高い評価を受けている[4)]。

このカメラシステム HEMS を用い2007年4月からすでに200例以上のセンチネルリンパ節生検を行い，センチネルリンパ節の同定率は100％を保っている。また，従来から行っていたインジゴカルミンを用いた色素法と99mTcスズコロイドを用いたRI法を同時に行い，HEMSの有用性について検討してきた。

今回は，近赤外線蛍光カラーカメラシステムHEMSを用いたICG近赤外線蛍光による乳癌センチネルリンパ節生検の実際の手技についてカラー写真を供覧して詳述する。

Ⅰ．Hyper eye medical system（HEMS）

HEMSはカメラ部分とそれを支えるアームおよび操作パネルを備えた本体とモニターから構成されている（図1a）。カメラ部分は超高感度CCDセンサーを入れた鏡体の前面に特殊レンズを中心にリング状に励起光を発するLEDを配列し，術野を照らすための手元照明としてそのリング内に4個の赤外線をカットしたLEDを配置している（図1b）。本体前面にある操作パネルは，レンズの焦点，ズーム，絞り，励起光および手元灯のオンオフと強弱の調節，SDカードへの録画

* Takeki SUGIMOTO 高知大学外科学講座外科1
*2 Kazuhiro HANAZAKI 同外科 教授
*3 Takayuki SATO 高知大学医学部 循環制御学 教授

key words
センチネルリンパ節生検，ICG近赤外線蛍光，カラー画像

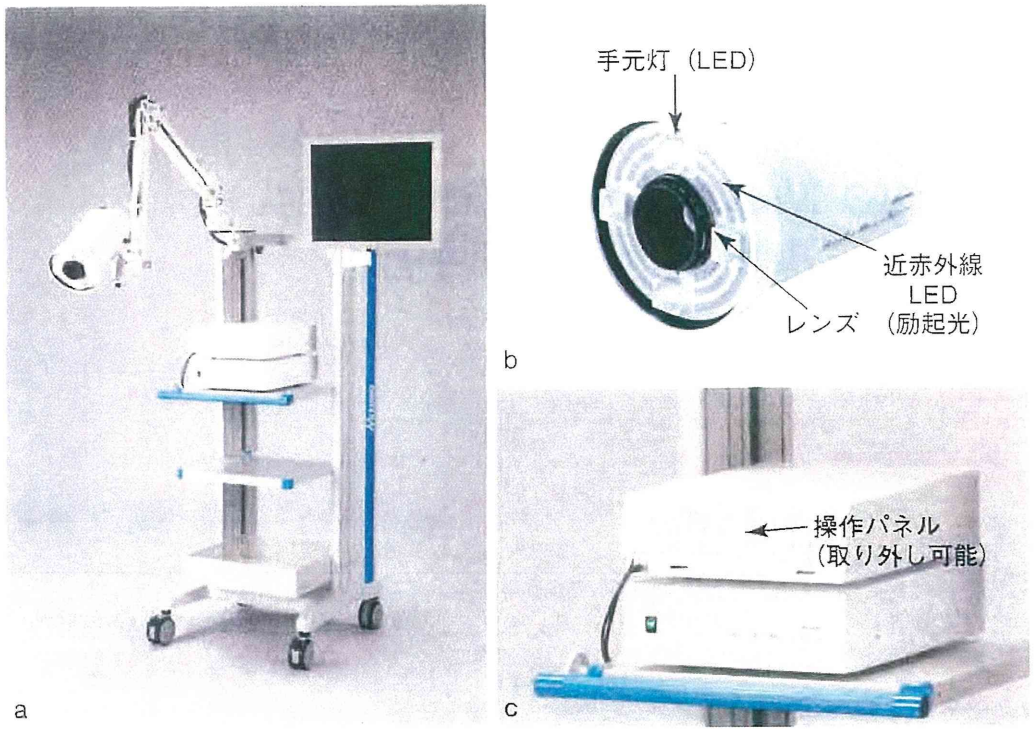

図1　近赤外蛍光カラーカメラシステム　Hyper eye medical system（HEMS）
a）HEMS概観。b）本体部分。c）カメラ部分。

図2　HEMSを用いたセンチネルリンパ節生検
HEMSのカメラは術者の肩越しに，術野から50 cm程度離れたところに設置している。

を操作することができる（図1c）。操作パネルは着脱が可能で，専用の清潔なドレープで覆うことで術野での操作も可能となっている。

Ⅱ．手術手技

1．術前処置

手術前日に乳輪縁皮下に99 mTcスズコロイドを注入し，手術開始前にガンマプローブを用いて約3 cm長の予定皮切線をマーキングする。

その後，消毒および敷布掛けを終えたのち，術者の肩越しにHEMSのカメラを設置し，ホワイトバランスの調節と設定位置でのカメラの焦点合わせを行う。HEMS本体に付属するモニターは主に助手および介助者用で，術者は外部出力ケーブルを接続し対側にモニターを設置して，その画面を見ながら手術を行うほうが手術操作はスムースである。HEMSのワーキング・ディスタンスは50 cm以上と長く，拡大機能があるため，近赤外蛍光の観察のためにカメラ自体を術野内に持ち込み術者もしくは助手が手で持って清潔操作を行う必要はない。

2．ICGの注入とリンパ管の観察

濃度5 mg/mlのICG 0.5～1 mlを3～4カ所に分け乳輪縁の皮膚直下に注入する。注入直後からカラーモニター上に腋窩に向かうリンパ管のルートが明視野で観察できる（図3a）。センチネルリンパ節の位置や個数を推定するために体外からより詳細にリンパ管の走行を観察する場面では暗視野が必要な場合もある。この段階では，手術室の照明を切って観察を行うこととしている（図3b）。HEMSの初期モデルで行った72例の検討では，95％がRI法でマーキングした予定皮切線

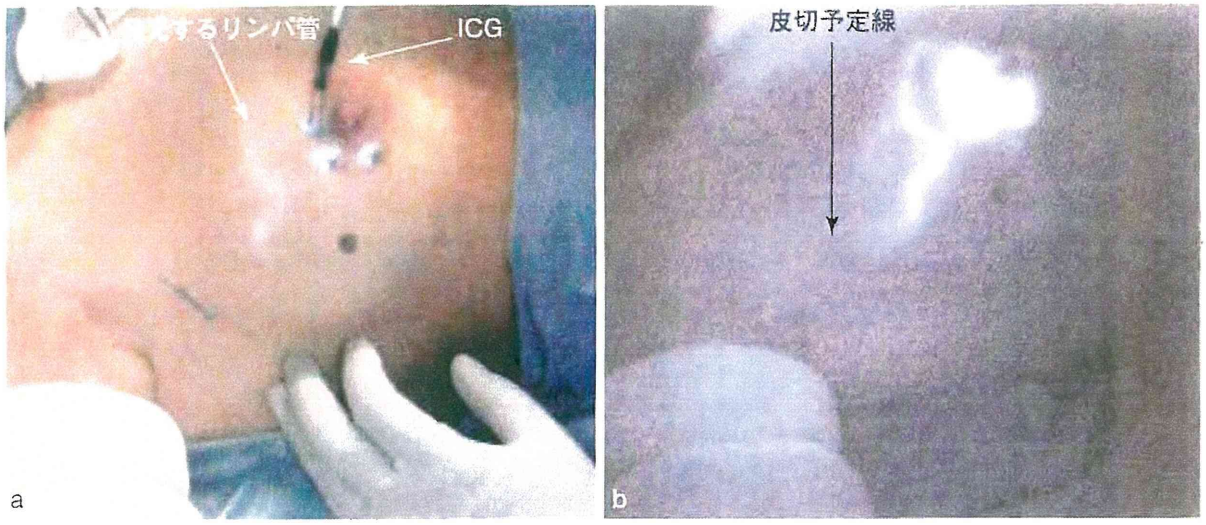

図3　インドシアニングリーン（ICG）の注入と体表からのリンパ管の観察

a）乳輪皮下にICGを注入中に，明視野でリンパ管が観察される。
b）暗視野ではより詳細なリンパ管の観察が行える。腋窩に向かうルートはラジオアイソトープ（RI）法でマークした皮膚切開予定線の直近まで体表から観察できる。

の2cm以内までリンパ管を観察することができている（未発表データ）。

3. 皮膚切開と皮下の処置

メスで約3cmの皮膚切開を入れたのち，電気メスで皮下の脂肪織を切開し，筋鉤で皮下組織を開排すると浅胸筋膜の表面が露出する。モニター上では筋膜の直下に発光する構造を認めるが，筋膜での反射により蛍光はぼんやりとしており，リンパ管やリンパ節そのものを同定することは困難である（図4）。この時点で，筋鉤を動かし，蛍光のもっとも強い部分を探し，そこで筋膜を切開する。

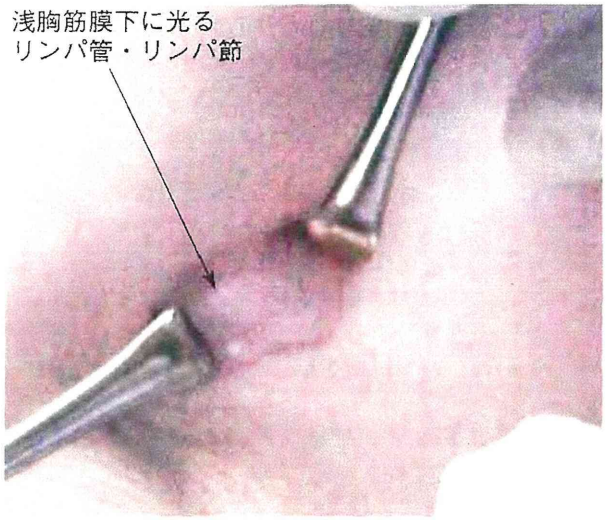

図4　浅胸筋膜の露出と筋膜上からの観察

皮膚切開および皮下脂肪を切離後，筋鉤で鈍的に開排すると浅胸筋膜下に発光するリンパ管・センチネルリンパ節をぼんやりと認める。

4. 流入リンパ管の検索と結紮・切離

浅胸筋膜を切開すると，索状に光るリンパ管が観察される（図5a）。多くの場合，この表層のリンパ管がセンチネルリンパ節への流入リンパ管である。そこで，このリンパ管を剝離鉗子で拾い上げ（図5b），遠位側（図5c），近位側ともに結紮したのち（図5d），これを剪刀で切離する。この流入リンパ管の結紮は創内へのICGの流出を予防し，周囲組織が色素で汚染され蛍光を発することがないようにするために必須の手技である。HEMSを用いるとモニター上で容易に流入リンパ管が同定でき，術野とモニターを交互に見ながら手術操作を行うことができる。

5. センチネルリンパ節の同定と摘出

本症例では2本目の流入リンパ管を認めたため，これも近位・遠位両側の結紮を行った後に切離している（図6a）。この結紮された遠位側のリンパ管を牽引しながら周囲組織を剝離していくとセンチネルリンパ節が発光体として認められる（図6b）。センチネルリンパ節を鉗子等で把持・牽引して（図6c），周囲組織を鋭的・鈍的に剝離し（図6d），センチネルリンパ節の摘出を行う。流出側にリンパ管が索状の蛍光体として認められ

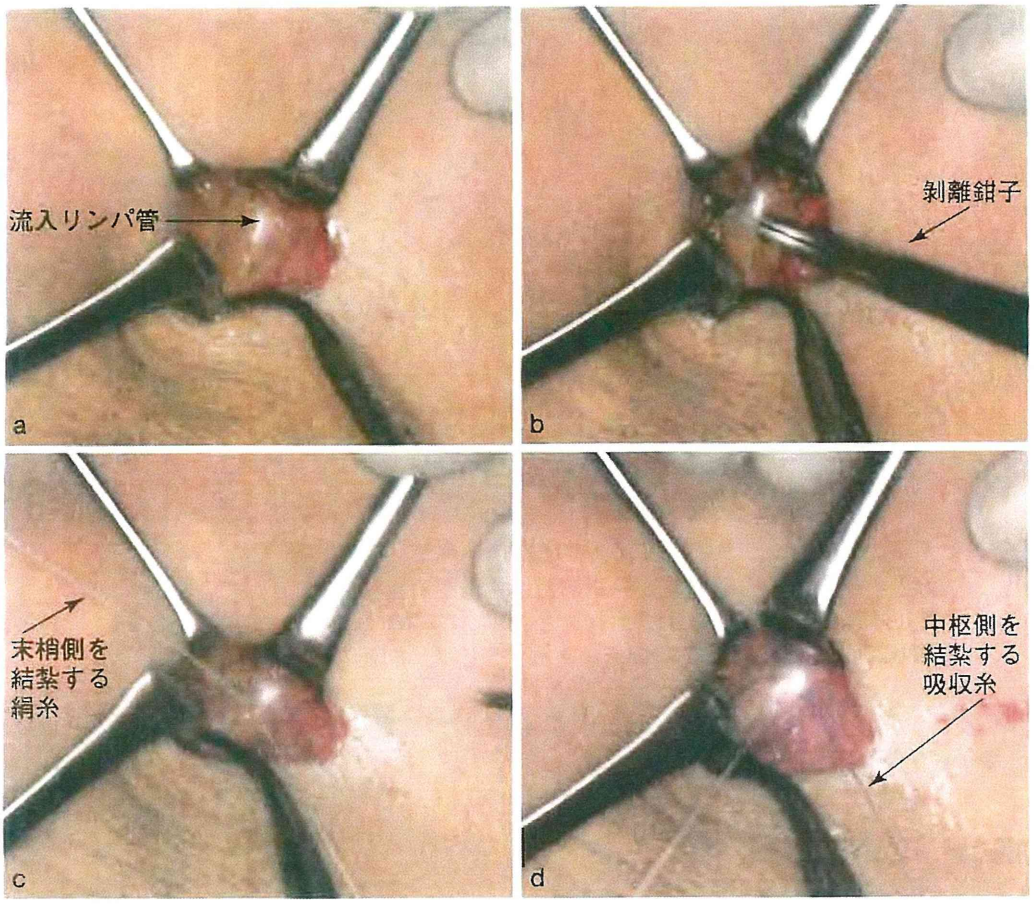

図5　流入リンパ管の結紮・切離

a）浅胸筋膜を切開し索状に発光するリンパ管を見出す。
b）リンパ管の裏側に剝離鉗子を通す。
c）リンパ管末梢側の結紮（絹糸）。
d）リンパ管中枢側の結紮（吸収糸）。

る場合は，流入リンパ管と同様，ICGによる術野の汚染を避けるため結紮・切離が必要なこともある。

6. センチネルリンパ節摘出後の確認

センチネルリンパ節摘出後は，創部とセンチネルリンパ節を同時にHEMSで観察し，創内にセンチネルリンパ節と同等に発光する構造がないことを確認し，センチネルリンパ節が複数でないことを確認する（図7）。この際，流入リンパ管を結紮した糸を動かし，近位側が体表から観察したリンパ管のメインルートと連続していること，また，より近位側にリンパ節がないことを確認する。これは，色素法の延長であるICG蛍光法で，センチネルリンパ節を通り抜けたICGによって蛍光を発しているセンチネル以外のリンパ節をセンチネルリンパ節と誤認しないためには必要な確認であると考えている。

当院では，切除されたセンチネルリンパ節は2 mmスライス毎に標本を作製し，術中迅速病理で転移の有無を判定している。転移陰性の場合は腋窩郭清を省略し，転移陽性の場合は皮膚切開を体格によって5〜7 cmまで延長しlevelⅡの腋窩リンパ節郭清を行っている。

創は浅胸筋膜と皮下を縫合後，真皮を5-0のモノフィラメント吸収糸で内翻縫合し，皮膚用ボンドで閉創している。

おわりに

近赤外線蛍光カラーカメラシステムは，ICG近赤外蛍光を利用した乳癌センチネルリンパ節生検において体表からのリンパ流の観察を容易にすると同時に，カラーモニター上で発光体であるリン

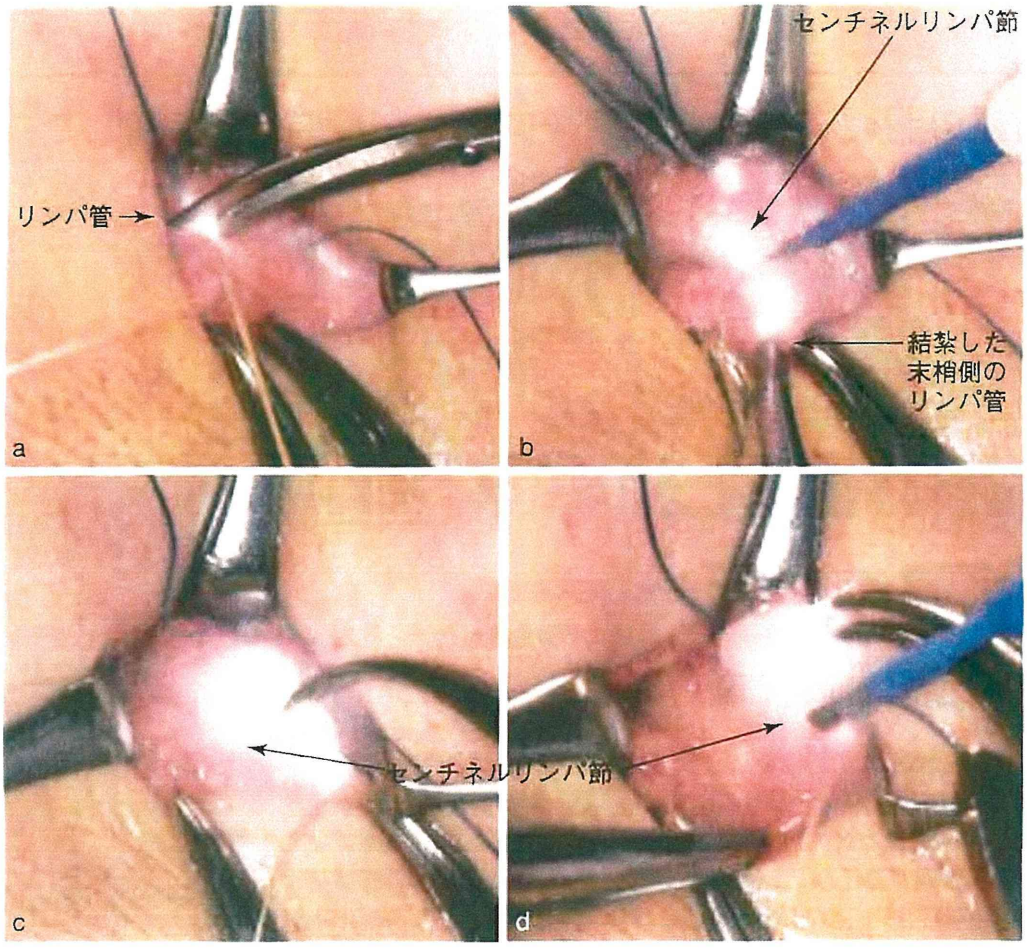

図6　センチネルリンパ節の同定と摘出

a）2本目の流入リンパ管の結紮・切離。
b）切離したリンパ管の末梢側を牽引しセンチネルリンパ節を発見。
c）センチネルリンパの補足と牽引。
d）センチネルリンパ節からの周囲組織の剝離。

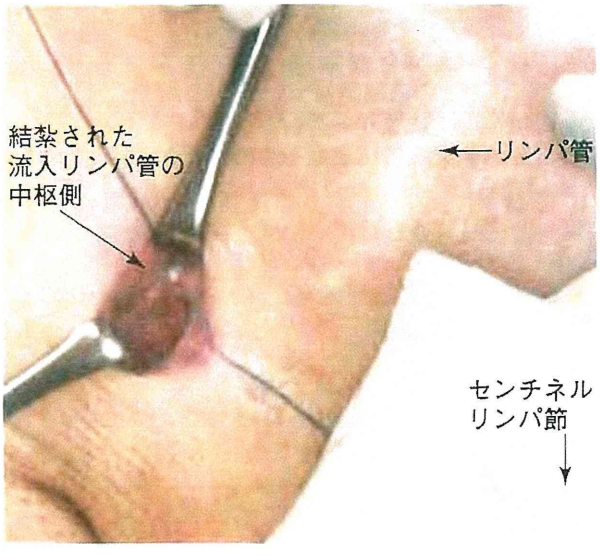

図7　センチネルリンパ節の摘出後

センチネルリンパ節摘出後，創内をHEMSで観察し発光する構造がないことと流入リンパ管の中枢側を確認する。

パ管・リンパ節と周囲組織の関係をリアルタイムに詳しく把握しながら手術操作が行える画期的な手術ナビゲーターである。

文献

1）Tagaya N et al : Intraoperative identification of sentinel lymph nodes by near-infrared fluorescence imaging in patients with breast cancer. Am J Surg 195 : 850-853, 2008
2）Ogasawara Y et al : Evaluation of breast lymphatic pathways with indocyanine green fluorescence imaging in patients with breast cancer. World J Surg 32 : 1924-1929, 2008
3）Handa T et al : New device for the intraoperative graft assessment : HyperEye charge-coupled device camera system. Gen Thorac Cardiovasc Surg 58 : 68-77, 2010
4）Marshall MV et al : Near-infrared fluorescence imaging in humans with indocyanine green: A review and update. Open Surg Oncol J 2 : 12-25, 2010

Beraprost sodium, a stable prostacyclin analogue, improves insulin resistance in high-fat diet-induced obese mice

Eriko Inoue[1], Toshihiro Ichiki[1,2], Kotaro Takeda[1,2], Hirohide Matsuura[1], Toru Hashimoto[1], Jiro Ikeda[1], Aya Kamiharaguchi[1] and Kenji Sunagawa[1]

Departments of [1]Cardiovascular Medicine and [2]Advanced Therapeutics for Cardiovascular Diseases, Kyushu University Graduate School of Medical Sciences, Fukuoka, Japan

(Correspondence should be addressed to T Ichiki at Department of Advanced Therapeutics for Cardiovascular Diseases, Kyushu University Graduate School of Medical Sciences; Email: ichiki@cardiol.med.kyushu-u.ac.jp)

Abstract

Obesity induces hypertrophy of adipocyte resulting in production of pro-inflammatory cytokines such as tumor necrosis factor-α (TNF-α) and monocyte chemoattractant protein 1 (MCP1 (CCL2)). These cytokines play an important role in the development of insulin resistance. Beraprost sodium (BPS), a prostaglandin I_2 analogue, is reported to attenuate inflammation. In this study, we examined the effect of BPS on glucose metabolism in mice fed a high-fat diet (HFD). Four-week-old C57/B6 male mice were fed a HFD for 12 weeks (HFD group) and the treatment group received oral BPS (300 μg/kg per day) for the same period. Then, glucose metabolism, histological changes, and gene expression of white adipose tissue (WAT) were examined. Body weight was increased, and glucose intolerance and insulin resistance were developed in the HFD group. Treatment with BPS improved glucose tolerance and insulin action without body weight change. Histological analysis of WAT showed an increase in the size of adipocyte and macrophage infiltration in the HFD group, which was attenuated by BPS treatment. BPS reduced HFD-induced expression of MCP1 and TNF-α in WAT. BPS also attenuated hepatic steatosis induced by the HFD. These results suggest that BPS improved glucose intolerance possibly through suppression of inflammatory cytokines in WAT. BPS may be beneficial for the treatment of obesity-associated glucose intolerance.

Journal of Endocrinology (2012) **213,** 285–291

Introduction

Obesity plays a central role in the development of metabolic syndrome (Wajchenberg 2000), a constellation of risk factors such as insulin resistance, dyslipidemia, and high blood pressure. Accumulation of visceral fat rather than subcutaneous fat is believed to cause insulin resistance (Wajchenberg 2000, Masuzaki *et al.* 2001). In obesity, adipocytes are enlarged and increased in number, and an excess of lipid leads to ectopic deposition of triglyceride in the liver and muscle, which is one of the causes of insulin resistance (Savage *et al.* 2007). The hypertrophied adipocytes produce proinflammatory cytokines such as monocyte chemoattractant protein-1 (MCP1 (CCL2)) and tumor necrosis factor-α (TNF-α) as obesity progresses (Shoelson *et al.* 2006). These cytokines, so-called adipokines, cause inflammation and recruitment of macrophages to adipose tissue (Xu *et al.* 2003), which is another important mechanism for obesity-induced insulin resistance. The infiltrated macrophages enhance inflammation of adipose tissue, indicating that these processes form a vicious circle.

TNF-α induces c-Jun amino-terminal kinase (JNK) activation and phosphorylation of insulin receptor substrate 1 (IRS1) at serine residues that negatively regulate normal signaling through the insulin receptor/IRS1 axis (Hotamisligil *et al.* 1996). Mice lacking chemokine receptor-2 (CCR2), a receptor for MCP1, are partly protected against developing high-fat diet (HFD)-induced insulin resistance and exhibit reductions in adipose tissue macrophage recruitment and inflammatory gene expression (Weisberg *et al.* 2006). These observations suggest that adipose tissue in obesity is characterized by chronic low-grade inflammation, and inflammatory cytokines play a causative role in the development of insulin resistance.

Beraprost sodium (BPS) is a stable prostaglandin I_2 analogue and has a potent vasodilating effect through activation of prostacyclin receptor (Olschewski *et al.* 2004). BPS is also reported to attenuate inflammation. BPS reduced serum TNF-α levels in diabetic patients (Fujiwara *et al.* 2004) and expression of *Mcp1* mRNA in the kidney of Otsuka Long-Evans Tokushima fatty (OLETF) rats, resulting in the amelioration of diabetic nephropathy (Watanabe *et al.* 2009). BPS inhibits

DOI: 10.1530/JOE-12-0014
0022–0795/12/0213–285 Online version via http://www.endocrinology-journals.org

TNF-α-induced expression of vascular cell adhesion molecule and monocyte attachment to endothelial cells (Goya *et al.* 2003). We therefore hypothesized that the anti-inflammatory effects of BPS may be beneficial for the improvement of obesity-induced insulin resistance, in which inflammation plays an important role.

We showed in this study that BPS improved glucose metabolism in association with reduction of inflammation of white adipose tissue (WAT) in a mouse model of diet-induced obesity.

Materials and Methods

Animals

All procedures were approved by the institutional animal use and care committee and were conducted in conformity with institutional guidelines. Four-week-old C57/B6 mice were purchased from Kyudo Co. Ltd. (Tosu, Saga, Japan). Three groups were analyzed: mice fed a normal chow diet (control group), mice fed a HFD containing 60% kcal fat (High Fat Diet 32, Clea Japan (Tokyo); HFD group) for 12 weeks, and mice fed a HFD and administered BPS for 12 weeks (BPS group). BPS dissolved in water at 1·5 μg/ml was given *ad libitum* because of the short half-life of BPS (~1 h). As a preliminary study showed that the estimated volume of water intake was ~0·2 ml/g per day, the estimated dose of orally ingested BPS was 300 μg/kg per day. At the end of the experiment, systolic blood pressure (SBP) and heart rate (HR) were measured by a tail-cuff method (BP-98A, Softron Co., Tokyo, Japan). Mice were killed by CO_2 inhalation.

Histological analysis

Adipose tissues were fixed with 10% formaldehyde for 24 h. The specimens were embedded into paraffin. Paraffin sections were stained with hematoxylin and eosin (H&E). The cross-sectional area for each adipocyte was determined using Dynamic cell count BZ-HIC (Keyence, Osaka, Japan). To detect macrophage infiltration, the paraffin sections were stained with an antimouse MAC3 (LAMP2) antibody (Santa Cruz Biotechnology, Inc., Santa Cruz, CA, USA). Sections were deparaffinized with xylene and refixed with ethanol for 40 min, immersed in PBS, and then autoclaved in citrate buffer for antigen retrieval. Then, the sections were incubated with 3% hydrogen peroxide in methanol for 20 min. The sections were further incubated with an antibody against MAC3 (1:200) overnight at 4 °C. After rinsing with PBS, the sections were incubated with biotin-labeled goat anti-rabbit IgG antiserum (Santa Cruz Biotechnology, Inc., 1:200 dilution) for 30 min and then incubated with avidin–biotin complex (Vectastain ABC kit; 1:100 dilution) for 15 min, and the sections were incubated with 3,3-diaminobenzidine and 0·03% hydrogen peroxide in deionized water for about 80 s. The number of MAC3-positive cell clusters was counted in high power field (HPF). The data are mean of five randomly chosen HPFs. After the mice were killed, the livers were removed and subsequently fixed in 10% formaldehyde. The sections were embedded in paraffin blocks and stained with H&E to examine the structures of the liver and evaluate lipid droplets. For the quantification of areas of lipid accumulation in the liver, H&E-stained images of liver were uploaded into a computer for analysis. The images were processed into two gradations (black and white). The white porosity areas were quantified as vacuolation (Sato *et al.* 2010), which mostly represents accumulation of lipid droplets. Contribution of arteries, veins, and bile ducts to porosity area was small and equally observed in the three groups and therefore ignored in the quantification. The data are expressed as a percentage of white area to total area.

Glucose tolerance test and insulin tolerance test

Mice were starved for 6 h. Then, the mice were i.p. injected with glucose (1 g/kg of body weight) for the glucose tolerance test (GTT). For the insulin tolerance test (ITT), the mice were i.p. injected with rapid insulin (0·5 IU/kg of body weight). Blood was taken from tail vein at various time points to measure blood glucose concentrations by Glutest Every (Sanwa Kagaku Kenkyusho, Nagoya, Japan).

Measurement of serum levels of triglyceride, cholesterol, and insulin

Serum triglyceride and total cholesterol levels were determined by commercially available kits, Triglyceride E-test Wako (Wako, Osaka, Japan) and Cholesterol E-test Wako (Wako) respectively. Serum insulin levels were determined by ELISA kit (Morinaga Institute of Biological Science, Yokohama, Japan).

RNA extraction and real-time quantitative RT-PCR analysis

RNA from adipose tissue was extracted using ISOGEN according to the manufacturer's instruction (Wako). One microgram of total RNA was reverse transcribed using ReverTra Ace qPCR RT Kit (Toyobo, Osaka, Japan). Real-time quantitative PCR (qPCR) was performed using 7500 real-time PCR system (Applied Biosystems) and SYBER Green PCR Master Mix (Applied Biosystems). Primer sequences for real-time qPCR used in this study are as follows:

TNF-α: 5′-AAGCCTGTAGCCCACGTCGTA-3′;
5′-GGCACCACTAGTTGGTTGTCTTTG-3′.
MCP1: 5′-TTAACGCCCCCACTCACCTGCTG-3′;
5′-GCTTCTTTGGGACACCTGCTGC-3′.
PPARγ (PPARG):
5′-TGTCGGTTTCAGAAGTGCCTTG-3′;
5′-TTCAGCTGGTCGATATCACTGGAG-3′.
C/EBPα: 5′-TTGAAGCACAATCGATCCATCC-3′;
5′-GCACACTGCCATTGCACAAG-3′.
Adiponectin: 5′-GTCAGTGGATCTGACGACACCAA-3′;
5′-ATGCCTGCCATCCAACCTG-3′.
18S rRNA: 5′-ACTCAACACGGGAAACCTCA-3′;
5′-AACCAGACAAATCGCTCCAC-3′.

The expression of each gene was normalized with that of *18s* rRNA.

ELISA

ELISA for adiponectin and TNF-α was performed using commercially available kits (R&D systems, Inc., Minneapolis, MN, USA) in accordance with the manufacturer's instructions.

Statistical analysis

Statistical analysis was performed with one-way ANOVA and Fisher's test if appropriate. Data are shown as mean±S.E.M. $P<0{\cdot}05$ was considered to be statistically significant.

Results

Hemodynamic and metabolic parameters

Body weight was significantly increased in the HFD group compared with the control group at the end of the experiment. However, there was no significant difference between the HFD and BPS groups (Table 1). SBP was significantly increased in the HFD group compared with the control group. BPS significantly reduced SBP, but SBP in the BPS group was still significantly higher than that in control group (Table 1). HR was significantly increased in the HFD group compared with the control group. BPS reduced HR, but the difference was not statistically significant (Table 1).

After 16 h of fasting, lipid profile and glucose and insulin levels were determined. Total cholesterol and triglyceride were significantly increased by the HFD (Table 2). BPS treatment modestly decreased total cholesterol and triglyceride levels. However, the differences were not statistically significant. Fasting insulin and glucose levels were elevated in the HFD group.

BPS improved GTT and ITT

At the end of experiment, GTTs and ITTs were performed. The HFD group developed glucose intolerance (Fig. 1A) and insulin resistance (Fig. 1C). Treatment of mice with BPS significantly improved glucose tolerance and insulin action (Fig. 1A and C). Interestingly, the basal glucose level was significantly lower in the BPS group compared with the HFD group after 6 h of fasting, which was not observed after 16 h of fasting (Table 2). Area under the curves (AUC) also showed improvement of glucose metabolism by BPS treatment (Fig. 1B and D).

Table 1 BW, SBP, and HR

	BW (g)	**SBP** (mmHg)	**HR** (b.p.m.)
Control ($n=5$)	26·9±0·5	97±3	448±31
HFD ($n=10$)	43·4±1·1†	114±2†	532±15†
HFD+BPS ($n=10$)	43·9±0·9†	106±2*,‡	496±15

HFD, high-fat diet; BPS, beraprost sodium; BW, body weight; SBP, systolic blood pressure; HR, heart rate. *$P<0{\cdot}05$, †$P<0{\cdot}01$ vs control. ‡$P<0{\cdot}05$ vs HFD group.

Table 2 Fasting serum chemistry of control, HFD-, and BPS-treated mice

	TC (mg/ml)	**TG** (mg/ml)	**Insulin** (ng/ml)	**Glucose** (mg/ml)
Control ($n=5$)	55±4	66±12	0·16±0·05	59·6±2·6
HFD ($n=10$)	209±9†	94±9*	3·75±0·51†	142·4±7·3†
HFD+BPS ($n=10$)	182±14†	74±6	4·12±0·90†	132·8±6·2†

HFD, high-fat diet; BPS, beraprost sodium; TC, total cholesterol; TG, triglyceride. *$P<0{\cdot}05$ and †$P<0{\cdot}01$ vs control.

BPS reduced adipocyte size

Histological analysis of epididymal WAT showed that the adipocyte size was increased in the HFD group compared with the control group (Fig. 2A and B). Treatment with BPS reduced adipocyte size (Fig. 2C). Statistical analysis confirmed that BPS significantly reduced adipocyte size (Fig. 2D). These data suggest that BPS enhanced adipocyte differentiation. We therefore examined expression of genes related to adipocyte differentiation. *Pparγ* was significantly suppressed by the HFD, which was reversed by BPS (Fig. 3A). The upregulation of *Pparγ* by BPS showed a borderline significance ($P=0{\cdot}06$) when three groups were considered. However, the difference between the HFD and BPS groups was statistically significant if only the HFD groups were compared ($P=0{\cdot}02$). We failed to see a significant effect of BPS treatment on the expression of C/EBPα (Fig. 3B) or adiponectin (Fig. 3C). Although adiponectin mRNA levels were not changed in the three groups, serum adiponectin levels were mildly decreased in the HFD group and BPS groups (Fig. 3D). However, the difference in serum adiponectin levels between the three groups was not statistically significant.

BPS reduced inflammatory changes in WAT in HFD-fed mice

Chronic inflammation in WAT is a common feature of obesity. Therefore, we examined the infiltration of macrophages into adipose tissue. The number of MAC3-positive macrophage aggregation surrounding adipocytes, often referred to as a crown-like structure (CLS) in WAT (Weisberg *et al.* 2003, Xu *et al.* 2003), was significantly increased in the HFD group compared with the control group (Fig. 2E and F; arrowheads). In the control group (Fig. 2E), almost no CLS was observed in WAT. Treatment with BPS significantly decreased the number of CLSs in WAT (Fig. 2G and H).

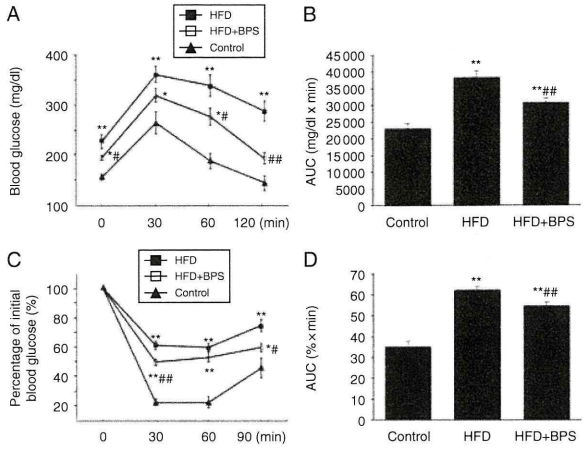

Figure 1 BPS ameliorated HFD-induced insulin resistance. (A) The control group (black triangle) was fed a normal chow and the HFD (black box) and BPS groups (white box) were fed a HFD for 12 weeks. Mice were i.p. injected with 1 g/kg glucose and blood glucose levels were measured. (C) Mice were i.p. injected with 0·5 U/kg insulin and blood glucose levels were measured. (B and D) AUC were calculated. Control group $n=5$, HFD group and BPS group $n=10$. $^{*}P<0{\cdot}05$ and $^{**}P<0{\cdot}01$ vs control. $^{\#}P<0{\cdot}05$ vs HFD group, $^{\#\#}P<0{\cdot}01$ vs HFD group.

Real-time PCR analysis showed that HFD-induced expression of TNF-α and MCP1 was significantly suppressed by BPS treatment (Fig. 3E and F). We could not detect serum TNF-α even in mice fed a HFD (data not shown).

BPS attenuated HFD-induced hepatic steatosis

Finally, we examined whether BPS affects hepatic steatosis induced by the HFD. HFD feeding for 12 weeks caused fatty liver compared with control feeding (Fig. 4A and B). Fat accumulation in the liver was attenuated in the BPS group compared with the HFD group (Fig. 4C and D).

Discussion

We demonstrated in this study that BPS improved HFD-induced insulin resistance and glucose intolerance. Treatment with BPS reduced expression of inflammatory cytokines, adipocyte size, and macrophage infiltration in WAT of diet-induced obesity mice. BPS also induced modest PPARγ upregulation. Although BPS treatment did not affect serum glucose and insulin levels after 16 h of fasting (Table 2), GTT performed after 6 h of fasting showed a significant reduction in basal glucose levels in the BPS group. The difference may be ascribed to the length of the fasting period, and prolonged fasting time may attenuate the difference between the HFD group and the BPS group.

Low-grade adipose tissue inflammation is a key state underlying insulin resistance in obesity. An increase in *TNF-α* mRNA expression was observed in adipose tissue from animal models of obesity and diabetes (Hotamisligil *et al.* 1993). It has been suggested that TNF-α is an important mediator of insulin resistance in obesity because neutralization of TNF-α increased peripheral glucose uptake in response to insulin in obese rats. And TNF-α-deficient obese mice were protected against obesity-induced attenuation of insulin signaling in muscle and fat tissues (Uysal *et al.* 1997). Several studies suggest that TNF-α blocks insulin signaling. It is reported that TNF-α inhibits insulin-induced tyrosine phosphorylation and tyrosine kinase activity of the insulin receptor in the obese rat (Hotamisligil *et al.* 1994*a*,*b*). TNF-α activates JNK signaling, and JNK activation promotes the

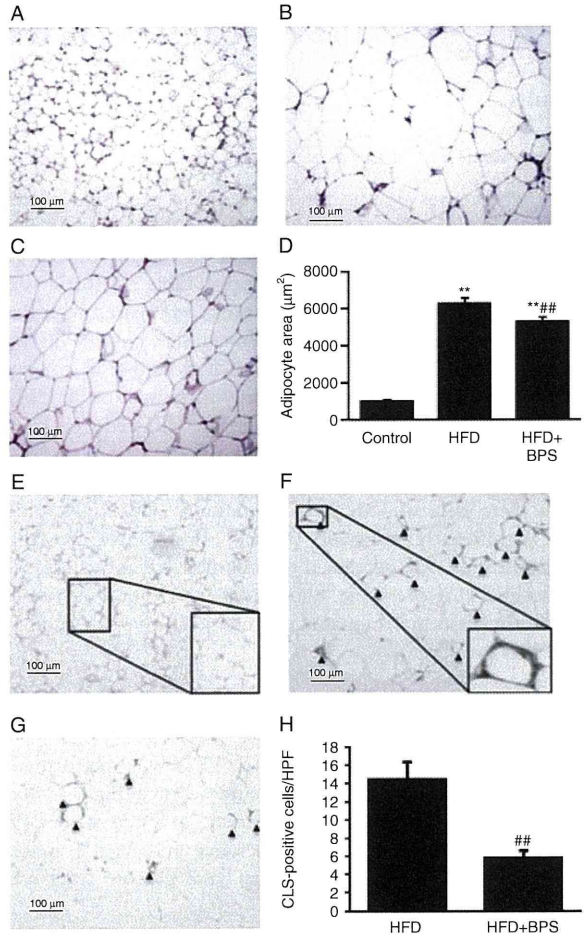

Figure 2 BPS treatment decreased adipocyte size and infiltration of macrophages in WAT. (A, B, and C) Representative microphotographs of H&E-stained sections of epididymal WAT from the control group (A), HFD group (B), and BPS group (C) are shown. Scale bar, 100 μm. (D) Bar graph indicates average adipocyte size of epididymal WAT, $n=5$ (control group; $n=3$). $^{**}P<0{\cdot}01$ vs control. $^{\#\#}P<0{\cdot}01$ vs HFD group. (E, F, and G) Representative microphotographs of WAT immunohistochemically stained with an anti-MAC3 antibody to stain macrophage in the control group (E), HFD group (F), and BPS group (G) are shown. Scale bar, 100 μm. (H) Bar graph indicates the number of CLSs in high power field (HPF), $n=7$–8. $^{\#\#}P<0{\cdot}01$ vs HFD group. Almost no CLS was observed in the control group.